Shape-optimization of a rigid cylinder for controlling flow-induced instabilities of a flexible splitter plate

Jean-Lou Pfister[a], Olivier Marquet[a]

[a] *ONERA – Paris Saclay University, 92190 Meudon, France*

Abstract

The oscillations of a flexible splitter plate interacting with the wake flow behind a rigid cylinder result from the destabilization of a fluid-elastic global mode [1]. An adjoint-based shape-optimization of the rigid cylinder is developed here, aiming at varying the eigenvalue associated to such fluid-elastic global mode. Two components are identified in the shape sensitivity function. The perturbative component accounts for the shape deformation in the unsteady equations governing the linear perturbation that develop around the steady base-flow. The base-flow component accounts for the shape deformation in the steady flow equations, that induces base-flow modification in the linear perturbation equations. The shape sensitivity functions, related to the growth rate and frequency of the unstable fluid-elastic global mode, are first discussed. For the frequency, the shape sensitivity is strongly dominated by the base-flow component and indicates that the rigid cylinder should be slendered to increase the oscillating frequency of the flexible plate. For the growth rate, the two components are of similar amplitude but of opposite trends, resulting in bell shapes to stabilize the fluid-elastic mode. Using this shape sensitivity functions, optimizations of the rigid cylinder's shape are then performed to control the flexible plate oscillation. When targeting independently a prescribed growth rate or frequency, very similar results are obtained. Slendering the rigid cylinder tends to stabilize the fluid-solid eigenmode and increase its frequency. With the objective of controlling the oscillation frequency of the flexible plate, we perform a shape optimization for an objective function minimizing the gap of both growth rate and frequency to target values. The shape of the rigid bodies leading to higher and lower frequency oscillations of the flexible plate are finally discussed and results are compared to time-marching simulations.

Keywords: fluid-structure interaction, shape optimization

Contents

1. Introduction

Many engineering configurations involve the interaction of a light structure with a fluid flow. In some cases, self-developing fluid-solid instabilities may develop [2]. These oscillations are sometimes desirable, for instance in mixing devices or music instruments, and sometimes undesirable, like the aeroelastic flutter of wings or bridge decks [3]. In many cases, a way to avoid oscillations or promote them in a specified way is to change the *shape* of the object, which is the object of the present paper.

When the flow features are simple (typically for high speed attached flows), fluid-elastic effects can be incorporated in a design approach in a relatively simple way by considering a quasi-static approach [3]. In that case, the shape optimization problem reduces to a structural optimization problem with external loads that model the influence of the flow [4]. This approach is however appropriate only in the case of simple flow topologies and a weak fluid-solid coupling. For more strongly coupled cases, for instance exhibiting large added-mass effects or vortex-induced vibrations, a fully coupled approach is required [?]. Recently, shape optimization in a strongly coupled setting have therefore been addressed. For instance Hur et al. [5] computed design sensitivities of a joined-wing aircraft represented by a beam model, by taking into account the feedback of airloads to the structure, while Lund et al. [6] computed the minimal drag shapes of a flexible object parametrized by NURBS curves in a steady viscous flow using a fully coupled approach. The same approach was followed more recently by Aghajari and Schäfer [7]. For all these cases, the gradient was computed using finite-differences. We rather consider here the case where all the mesh points of the boundary of interest are to be optimized, because this avoids to define an *a-priori* parametrization of the geometry. In this case, the finite-difference approach ceases to be optimal, in favor of adjoint-based approaches [8, 9], that will be adopted here.

The key point is then to obtain the adjoint fluid-solid problem at the continuous level, for it allows to obtain an explicit formula for the shape gradient [10]. If the pure hydrodynamics case is well known for long [9, 11], this is quite a tedious task in the fluid-elastic context, which pushed in the past for considering approximate approaches where the geometrical couplings are neglected [12, 13]. In particular, whithin the so-called *frozen domain velocity* approximation [14, 15, 16], time-dependant Arbitrary-Lagrangien Eulerian (ALE) adjoint equations are relatively easily obtained by assuming that the time-dynamics of the flow is much faster than the mesh movement dynamics. Under this assumption (whose physical meaning does not seem to be really clear [retrouver qui avait dit ca]), the sensitivity to the domain displacement is simply obtained as a post-processing [15], but the coupling is not considered in a fully consistent way. To our knowledge, a continuous adjoint ALE equation was obtained in a fully coupled setting for a stationary Stokes flow coupled with a chord model by [17], for the purpose of goal-oriented error estimation, while the first attempt for deriving then solving a fully coupled fluid-structure adjoint problem was done by [18], using an Eulerian-based linearization of the fluid-structure equations [19, 20]. The authors derived an adjoint fluid-structure problem for an unsteady Stokes flow interacting with a one-dimensional Koiter solid model. Their derivation resulted in an unsteady Stokes problem backward in time and expressed in the deformed configuration, coupled with the solid model through a rather complicated interface term,

that was found to depend on the adjoint flow field and on the geometric properties of the interface. The authors used then the adjoint equations to solve a shape optimization problem inspired by haemodynamics concerns. In this work, we rather adopt a Lagrangian-based linearization approach [21, 22, 23] for deriving a shape gradient formula in the fully coupled case, because it results in a more favorable structure for the adjoint problem [voir aussi [24] and [17] for the Lagrangian-based/Eulerian-based approaches comparisons].

As evoked above, we wish to control unsteadiness in the fluid-solid shape optimization. They have for instance already been considered by [25], who used an adjoint-based method coupled with an Euler solver to optimize the shape of a rigid airfoil undergoing a *prescribed* oscillation, in order to minimize its time-average coefficient of drag. Drag reductions as high as 46 % have been obtained while maintaining the time-averaged lift coefficient. In the context of micro-air vehicle design, [26] used a vortex-lattice aerodynamic model coupled with a plate finite-element model to compute optimal *forced* flapping wing design. To our knowledge, only few attempts for taking into account a *self-developping* unsteadiness (not forced) in the flow about a structure to be optimized were done. In the context of pure hydrodynamics, one can mention the work by [27] were the geometry is parametrized by a few points, and that by [28] who used an adjoint-based approach without an *a-priori* parametrization of the shape. For both case, efforts are put on the stabilization of an unstable mode developing on the steady viscous Navier-Stokes solution, in the case of a rigid geometry. More recently, Wang et al. [29] performed the shape optimization of a sudden contraction channel flow and found that rounded corners allows stabilizing the real eigenmode responsible for the flow asymmetry. The continuous shape sensitivity function of the unstable eigenmode responsible for the vortex-shedding in the wake of a circular cylinder wake flow was recently derived and discussed by Brewster & Juniper [30]. Martinez et al. [31] proposed a discrete framework to obtain the shape sensitivity function of eigenmodes computed for compressible and turbulent flows modelled with RANS equations. They applied that formalism to modify the shape of a NACA0012 airfoil so as to damp the complex eigenmodes responsible for the shock oscillation.

In the present work, we follow such a strategy of shape optimization accounting for fluctuations using linear stability analysis and we extend it to fluid-structure interaction problems with an elastic structures. The Arbitrary Langrangian Eulerian framework is used the coupling of the (incompressible) fluid and (elastic) structure governing equations. The linearization of these equations and the eigenvalue problem formulation relies on the framework exposed in [23]. The linear and nonlinear dynamics of the flexible splitter plate clamped to the rigid cylinder is described in [1] when varying the elastic stiffness. The latter is chosen so that a fluid-elastic eigenmode is unstable. A shape-optimization of the rigid cylinder is performed aiming at modyfying either

modyfying the After deriThe continuous shape-optimization framework is using such optimisation

In the following sections, we first state the optimization problem. The governing state and adjoint equations are then presented, and details on the numerical method are given. The approach is used to control a classical problem in computational fluid-structure interaction, i.e. that of the self-developping oscillations of a plate clamped behind a cylinder, interacting with a low-Reynolds number flow [32]. In a recent study [Pfister-Marquet JFM 20xx], found unstable eigenmodes responsible for the development of these flow-induced vibrations. We consider the shape optimization of the rigid cylinder. After having presented the shape gradient, the shape optimization is carried out, first for stabilizing the mode, and then to modify the unstable vibration frequency of the system.

2. Problem setting

2.1. Geometry and non-dimensional parameters

The geometry of the present fluid-structure configuration is taken from a study by [Pfister-Marquet JFM 20xx] and is reproduced in the Fig. 1, where we have indicated the non-dimensional lengths. An elastic plate of length L^* and thickness H^* is clamped on the rear side of a *rigid* circular cylinder of diameter D^*. The non-dimensional length of the plate is set to $L^*/D^* = 2$ and the thickness to

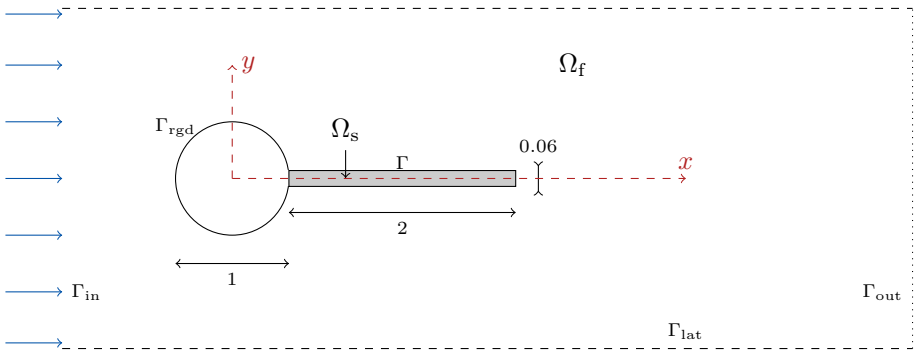

Figure 1: Geometry of the problem. Represented with dimensionless lengths relative to the cylinder's diameter.

$H^*/D^* = 0.06$. The cylinder's boundary Γ_rgd is rigid, while the fluid-elastic boundary Γ deforms under the action of the fluid.

A uniform flow field of velocity U^*_∞ is applied at the inlet of the domain. We assume that the viscous flow of density ρ^*_f and viscosity η^*_f is incompressible. For short splitter plates, the cylinder diameter D^* is an appropriate measure of the characteristic length scale in the flow, while the inflow velocity is taken as the characteristic velocity. We assume that the solid has the same density as that of the fluid, i.e. $\rho^*_\mathrm{s} = \rho^*_\mathrm{f}$. The homogeneous, isotropic solid is characterized by its Young modulus E^*_s and Poisson coefficient ν_s that is fixed to 0.35. Four non-dimensional parameters then govern the fluid-elastic problem, namely

$$\mathcal{R}_\mathrm{e} = \frac{\rho^*_\mathrm{f}\, U^*_\infty D^*}{\eta^*_\mathrm{f}}\,, \qquad \mathcal{M}_\mathrm{s} = \frac{\rho^*_\mathrm{s}}{\rho^*_\mathrm{f}} = 1\,, \qquad \mathcal{E}_s = \frac{E^*_\mathrm{s}}{\rho^*_\mathrm{f}\,(U^*_\infty)^2} \qquad \text{and} \qquad \nu_\mathrm{s} = 0.35.$$

for the Reynolds number, the (fixed) density ratio, the non-dimensional Young modulus and the (fixed) Poisson coefficient, respectively.

2.2. Time-linearised fluid-elastic vibrations over a Navier-Stokes steady flow

In this study, we analyse the evolution of small fluid-elastic perturbations developing over a steady-state equilibrium in which the solid deformations are neglected. In the present case, it has been shown [Pfister & Marquet JFM] that the steady deformations of the splitter plate remain indeed negligible as long as the rigidity is chosen high enough, which will be the case here: preliminary computations showed that the plate undergoes a slight compression associated to displacements not greater than 10^{-5}. The coupled fluid/elastic state vector $\boldsymbol{q}(\boldsymbol{x},t)$ is thus split as follows:

$$\boldsymbol{q}(\boldsymbol{x},t) = \boldsymbol{Q}(\boldsymbol{x}) + \varepsilon\,\mathfrak{Re}\big\{\boldsymbol{q}^\circ(\boldsymbol{x})\,\exp((\lambda^r + \mathbf{i}\lambda^i)t)\big\} + \circ(\varepsilon). \tag{1}$$

In this decomposition, the steady component $\boldsymbol{Q}(\boldsymbol{x})$ corresponds to the steady Navier-Stokes flow of velocity $\boldsymbol{U}(\boldsymbol{x})$ and pressure $P(\boldsymbol{x})$ about the *rigid* geometry. As mentioned above, this approximation is valid as long as the steady displacements remain indeed small, as is the case for the present configuration. The fluid velocity and pressure are then solution of the Navier–Stokes equations

$$(\nabla\boldsymbol{U})\,\boldsymbol{U} - \nabla\cdot\boldsymbol{\sigma}(\boldsymbol{U},P) = 0, \qquad -\nabla\cdot\boldsymbol{U} = 0 \qquad \text{in } \Omega_\mathrm{f}, \tag{2}$$

$$-\boldsymbol{U} = \boldsymbol{0} \qquad \text{on } \Gamma_\mathrm{rgd}\cup\Gamma, \tag{3}$$

where $\boldsymbol{\sigma}(\boldsymbol{U},P) = -P\,\mathbf{I} + 2/\mathcal{R}_\mathrm{e}\,(\nabla\boldsymbol{U} + \nabla\boldsymbol{U}^\mathrm{T})$ is the fluid viscous stress tensor. The farfield boundary conditions are taken as follows: an inflow condition $\boldsymbol{U} = \boldsymbol{U}_\mathrm{in}$ is prescribed on Γ_in, a stress-free outflow condition $\boldsymbol{\sigma}(\boldsymbol{U},P)\boldsymbol{n} = 0$ is prescribed on Γ_out, and we consider finally a slip condition $\boldsymbol{U}\cdot\boldsymbol{n} = 0$, $\boldsymbol{\sigma}(\boldsymbol{U},P)\boldsymbol{n}\cdot\boldsymbol{t} = 0$ (with $\boldsymbol{t}$ the tangential vector) on the side boundaries Γ_lat [33].

The unsteady component $\boldsymbol{q}^\circ(\boldsymbol{x})\exp(\lambda\,t)$, with $\lambda = \lambda^r + \mathbf{i}\lambda^i$, is the complex linear perturbation field taken under the form of the most unstable global mode [34] found over the steady equilibrium. A case with $\lambda^r < 0$ means that a small perturbation to $\boldsymbol{Q}(\boldsymbol{x})$ will eventually decay exponentially, while $\lambda^r > 0$

means that this perturbation is exponentially amplified, leading to the development of an unsteady flow with structural vibrations at the frequency λ^i, at least during the linear phase of the instabilities. Unlike for the steady component, fluid-elastic vibrations are taken into account there. The grouped field $\boldsymbol{q}^\circ(\boldsymbol{x})$ thus regroups the fluid velocity $\boldsymbol{u}^\circ(\boldsymbol{x})$ and pressure $p^\circ(\boldsymbol{x})$ perturbations modes, as well as a displacement perturbation mode $\boldsymbol{\xi}^\circ(\boldsymbol{x})$. The Arbitrary Lagrangian Eulerian approach [35, 36] has been considered to derive the linear evolution equations for the fluid-solid perturbations. Within this framework, it has been shown by Pfister et al. [23] that the perturbation problem reads on the form of a linearised problem coupling the solid and the fluid dynamics by means of an *extension fields* used to propagate the solid displacement onto the fluid domain. The equations for the solid dynamics are

$$\lambda\,\mathcal{M}_\mathrm{s}\,\boldsymbol{u}_s^\circ - \nabla\cdot\boldsymbol{\sigma}_\mathrm{s}(\boldsymbol{\xi}^\circ) = 0 \qquad \text{in} \quad \Omega_\mathrm{s}, \tag{4}$$

$$\lambda\,\boldsymbol{\xi}^\circ - \boldsymbol{u}_s^\circ = 0 \qquad \text{in} \quad \Omega_\mathrm{s}, \tag{5}$$

where $\boldsymbol{u}_s^\circ$ is the solid velocity, introduced so as to obtain a problem that is first-order in time, i.e. a linear eigenvalue problem. The solid infinitesimal stress tensor writes as

$$\boldsymbol{\sigma}_\mathrm{s}(\boldsymbol{\xi}^\circ) = \frac{\mathcal{E}_s}{1+\nu_\mathrm{s}}\left\{\frac{\nu_\mathrm{s}}{1-2\nu_\mathrm{s}}(\nabla\cdot\boldsymbol{\xi}^\circ)\,\mathbf{I} + \nabla\boldsymbol{\xi}^\circ + \nabla\boldsymbol{\xi}^{\circ\,\mathrm{T}}\right\}.$$

The fluid velocity and pressure perturbations, $\boldsymbol{u}^\circ$ and p°, satisfy the the linearised Navier-Stokes equations. Because of the movement of the solid, the position of the fluid domain is also perturbed, by means of the extension displacement field $\boldsymbol{\xi}_e^\circ$. The resulting equations write as

$$\lambda\left(\boldsymbol{u}^\circ - (\nabla\boldsymbol{U})\,\boldsymbol{\xi}_e^\circ\right) + (\nabla\boldsymbol{U})\left(\boldsymbol{u}^\circ + \boldsymbol{\Phi}'(\boldsymbol{\xi}_e^\circ)\,\boldsymbol{U}\right) + (\nabla\boldsymbol{u}^\circ)\boldsymbol{U}\cdots \tag{6}$$

$$-\nabla\cdot\left[\boldsymbol{\Sigma}'(\boldsymbol{\xi}_e^\circ,\boldsymbol{U},P) + \boldsymbol{\sigma}(\boldsymbol{u}^\circ,p^\circ)\right] = \mathbf{0} \qquad \text{in} \quad \Omega_\mathrm{f}, \tag{7}$$

$$-\nabla\cdot\boldsymbol{u}^\circ - \nabla\cdot\left(\boldsymbol{\Phi}'(\boldsymbol{\xi}_e^\circ)\,\boldsymbol{U}\right) = 0 \qquad \text{in} \quad \Omega_\mathrm{f}, \tag{8}$$

$$-\boldsymbol{u}^\circ = \mathbf{0} \qquad \text{on} \quad \Gamma_\mathrm{rgd}, \tag{9}$$

where the first equation is the momentum equation, and the second equation the continuity equation. The tensor $\boldsymbol{\sigma}(\boldsymbol{u}^\circ,p^\circ)$ is the usual viscous stress tensor already introduced above, while $\boldsymbol{\Phi}'(\boldsymbol{\xi}_e^\circ) = \nabla\cdot\boldsymbol{\xi}_e^\circ\,\mathbf{I} - \nabla\boldsymbol{\xi}_e^\circ$ is a deformation operator, and

$$\boldsymbol{\Sigma}'(\boldsymbol{\xi}_e^\circ,\boldsymbol{U},P) = \boldsymbol{\sigma}(\boldsymbol{U},P)\boldsymbol{\Phi}'(\boldsymbol{\xi}_e^\circ)^\mathrm{T} - \frac{1}{\mathcal{R}_\mathrm{e}}\left\{\nabla\boldsymbol{U}\nabla\boldsymbol{\xi}_e^\circ + \nabla\boldsymbol{\xi}_e^{\circ\,\mathrm{T}}\nabla\boldsymbol{U}^\mathrm{T}\right\}$$

expresses how the fluid stresses are modified by the perturbation of the domain. These equations are completed by the zero-velocity condition $\boldsymbol{u}^\circ = \mathbf{0}$ on $\Gamma_\mathrm{in}\cup\Gamma_\mathrm{rgd}$, a slip condition $\boldsymbol{u}^\circ\cdot\boldsymbol{n}_\mathrm{f}$ on the side boundaries and a stress-free outflow condition $\boldsymbol{\sigma}(\boldsymbol{u}^\circ,p^\circ)\boldsymbol{n}_\mathrm{f} = \mathbf{0}$ on Γ_out — as will be detailed later, we assume that far from the solid, the extension variable as well as its derivatives are identically zero, and especially $\boldsymbol{\Sigma}'(\boldsymbol{\xi}_e^\circ,\boldsymbol{U},P) = \mathbf{0}$ on Γ_out. Eventually, the fluid equations (7) and (8) are coupled to the solid equations (4) and (5) by means of displacement, velocity and stress interface conditions on the common interface Γ, namely

$$\boldsymbol{\xi}^\circ - \boldsymbol{\xi}_e^\circ = \mathbf{0} \qquad \text{on} \quad \Gamma, \tag{10}$$

$$\lambda\,\boldsymbol{\xi}^\circ - \boldsymbol{u}^\circ = \mathbf{0} \qquad \text{on} \quad \Gamma, \tag{11}$$

$$\left[\boldsymbol{\sigma}(\boldsymbol{u}^\circ,p^\circ) + \boldsymbol{\Sigma}'(\boldsymbol{\xi}_e^\circ,\boldsymbol{U},P)\right]\boldsymbol{n} = \boldsymbol{\sigma}_\mathrm{s}(\boldsymbol{\xi}^\circ)\,\boldsymbol{n} \qquad \text{on} \quad \Gamma, \tag{12}$$

while the extension displacement field $\boldsymbol{\xi}_e^\circ$ used to extend the solid displacement on the fluid domain is defined as

$$-\nabla^2\boldsymbol{\xi}_e^\circ = \mathbf{0} \qquad \text{in} \quad \Omega_\mathrm{e} \qquad \text{and} \qquad \boldsymbol{\xi}_e^\circ = \mathbf{0} \quad \text{in} \quad \Omega_\mathrm{f}\setminus\Omega_\mathrm{e}, \tag{13}$$

where Ω_e is the extension domain, defined as a subset of Ω_f located in the vicinity of the fluid-solid interface Γ. In order to prevent from having to distinguish Ω_f from Ω_e, the extension field is defined over Ω_f and is continuously extended into a zero field outside from Ω_e [pas clair ?!]. The system of fluid

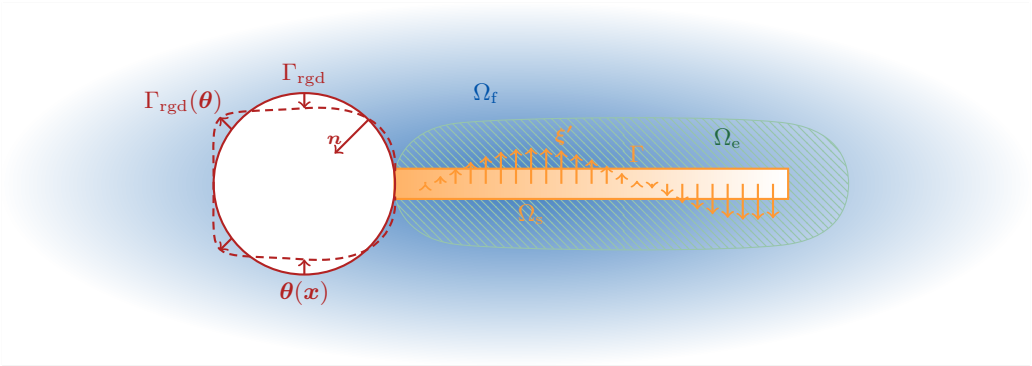

Figure 2

equations (4), (5), solid equations (7), (8), and coupling conditions (10), (11), (12), and (13) form an eigenvalue problem describing fully coupled fluid-solid perturbations developing over a steady flow over a rigid object. This problem admits several pairs of complex-conjugate eigenvalues as solutions, but only one is of interest here, the one that has the largest growth-rate. This eigenvalue corresponds indeed to the mode that becomes predominant over the other modes when $t \to \infty$. For that reason, in all what follows, it should be always understood that the pair $\{\lambda^r + \mathbf{i}\lambda^i; \boldsymbol{q}^\circ\}$ corresponds to the mode having the largest growth-rate (leading mode).

2.3. Fluid-elastic shape sensitivity

We address the problem to find which shape stabilizes or destabilizes the perturbations, or modifies the frequency of unstable fluid-solid oscillations in a prescribed way — under the constraints formed by the stationary Navier-Stokes flow and the fluid-elastic eigenvalue problem. A first step towards this consists in determining the shape *sensitivity* of an eigenvalue to domain changes, i.e. what kind of shape deformation would affect the growth-rate or the frequency of the mode. The main results are given below, while the complete derivation is reported in Appendix A.

In spirit, the derivation of the sensitivity formula follows closely the work by Marquet et al. [37], who derived in a pure hydrodynamics context the sensitivity of an eigenvalue to steady flow modifications and to a steady force. In the present case, the control parameter is a geometrical boundary rather than some abstract distributed momentum forcing term. We rely here on a Lagrangian parametrization [38, 10, 39] for representing the variations of the boundary Γ (and thus the domain Ω), namely

$$\Omega(\boldsymbol{\theta}) = (\mathrm{Id} + \boldsymbol{\theta})(\Omega) \qquad \text{and} \qquad \Gamma_{\rm rgd}(\boldsymbol{\theta}) = (\mathrm{Id} + \boldsymbol{\theta})(\Gamma_{\rm rgd}) \tag{14}$$

where $\boldsymbol{\theta}$ is a smooth, one-to-one field [38] used to deform the fluid-solid domain, as visualised on the sketch in Fig. 2. From now on, we note $\Omega = \Omega(\mathbf{0})$ and $\Gamma_{\rm rgd} = \Gamma_{\rm rgd}(\mathbf{0})$ the non-deformed boundaries. Note that the fluid-solid boundary is *not* modified through the optimization process, since $\Gamma \cup \Gamma_{\rm rgd} = \emptyset$. The solid domain $\Omega_{\rm s}$ is then independent from $\boldsymbol{\theta}$. For convenience, we choose an extension domain that encloses the solid domain in such a way that is is also independent from $\boldsymbol{\theta}$ (see Fig. 2). The *shape derivative* of the complex eigenvalue λ is then defined as the Fréchet derivative of the underlying mapping $\boldsymbol{\theta} \mapsto \lambda(\boldsymbol{\theta})$ at $\boldsymbol{\theta} = \mathbf{0}$, i.e.

$$\lambda(\boldsymbol{\theta}) = \lambda(0) + \lambda'(\Gamma_{\rm rgd})(\boldsymbol{\theta}) + \circ(\boldsymbol{\theta}). \tag{15}$$

Note that the complex numbers are viewed here as vectorial functions with values in $\mathbb{R}^2$. The so-called *structure theorem* obtained from the theory of geometric shape optimization [38, 10, 39] then gives that the shape derivatives has the following structure:

$$\lambda'(\Gamma_{\rm rgd})(\boldsymbol{\theta}) = \int_{\Gamma_{\rm rgd}} G_\lambda \, \boldsymbol{\theta} \cdot \boldsymbol{n} \, \mathrm{d}\Gamma \qquad \forall \boldsymbol{\theta}. \tag{16}$$

In particular, $\lambda'(\Gamma_{\rm rgd})(\boldsymbol{\theta})$ depends only on the normal component $\boldsymbol{\theta} \cdot \boldsymbol{n}$, reflecting the intuitive idea that variations of a border along the normals affect the domain at first order, while tangential variations

have only a higher-order influence. The (yet unknown, complex-valued) function G_λ is derived using a Lagrangian approach initially proposed by Céa [40], that allows to turn the constrained optimization problem (by the steady and perturbation problem) into an unconstrained problem. In the present case, we obtain (see the detail of the derivation in Appendix A)

$$G_\lambda = \frac{2}{\mathcal{R}_\mathrm{e}}\Big\{\mathbf{D}(\boldsymbol{U}) : \mathbf{D}(\overline{\boldsymbol{U}}^\dagger) + \mathbf{D}(\boldsymbol{u}^\circ) : \mathbf{D}(\overline{\boldsymbol{u}}^\dagger)\Big\} \qquad \text{on} \qquad \Gamma_\mathrm{rgd}. \tag{17}$$

where $\mathbf{D} = 1/2\,(\nabla + \nabla^\mathrm{T})$, and $\mathbf{A} : \mathbf{B} = A_{ij}B_{ij}$. Similarly to what was found by [37], the growth-rate and frequency shape sensitivities are obtained respectively from $\mathfrak{Re}\{G_\lambda\}$ and $\mathfrak{Im}\{G_\lambda\}$ [vérifier le signe de la partie imag]. The gradient depends on the derivatives of the steady flow velocity $\boldsymbol{U}$ and perturbation velocity $\boldsymbol{u}^\circ$, as well as on *adjoint* fields $\boldsymbol{U}^\dagger$ and $\boldsymbol{u}^\dagger$ that will be explicited in the following. In the above formula, G_λ has only a normal component The presence of two components in the gradient results from the fact that the sensitivity of the eigenvalue with respect to a domain variation actually depends on two mechanisms. We can indeed write $\lambda = \lambda(\Omega, \boldsymbol{Q}(\Omega))$. The first argument refers to the fact that, for a given $\boldsymbol{Q}$, the structure of the eigenvalue problem is obviously affected by a variation of the domain Ω. The second argument expresses that the stationary flow $\boldsymbol{Q}$ is itself a function of Ω through the stationary problem. Considering a variation $\delta\boldsymbol{\theta}$ of the domain mapping, a corresponding variation $\delta\lambda$ of the eigenvalue can therefore be formally written, with the appropriate scalar products $(\cdot,\cdot)$

$$\delta\lambda = (\nabla_\Omega\lambda, \delta\boldsymbol{\theta}) + (\nabla_{\boldsymbol{Q}}\lambda, \delta\boldsymbol{Q})\,.$$

The first term is related to how a modification of the domain influences the cost-function, for a *fixed* stationary flow. This term is thus related to mechanisms that influence the eigenvalue through linear, unsteady mechanisms. On the other hand, the second term is related to the influence of the variations of the steady flow through a modification of the geometry.

Let us now detail the equations required to compute the fields involved in the shape gradient formula (17).

2.3.1. Adjoint perturbation equations

The adjoint equations are obtained by differentiating the Lagrangian function for the optimization problem with respect to the direct perturbation variables. Details on the derivation are reported in Appendix A. Adjoint equations for the solid dynamics write as follows:

$$\overline{\lambda}\,\boldsymbol{\xi}^\dagger - \nabla\cdot\boldsymbol{\sigma}_\mathrm{s}(\boldsymbol{u}_s^\dagger) = 0 \qquad \text{in } \Omega_\mathrm{s}, \tag{18}$$

$$\overline{\lambda}\,\mathcal{M}_\mathrm{s}\,\boldsymbol{u}_s^\dagger - \boldsymbol{\xi}^\dagger = 0 \qquad \text{in } \Omega_\mathrm{s}. \tag{19}$$

These equations take a structure similar to the direct solid vibration problem (4)–(5). In particular, eliminating the adjoint displacement variable $\boldsymbol{\xi}^\dagger$ in (18) shows that the solid problem without augmentation is self-adjoint with respect to the scalar product derived from the energy norm, as is always the case for solid vibration problems in absence of damping [41]. The adjoint velocity $\boldsymbol{u}_s^\dagger$ should therefore be understood as the variable adjoint to the solid displacement $\boldsymbol{\xi}^\circ$. The adjoint equations for the fluid dynamics take exactly the same form than that obtained in the pure hydrodynamics case [42, 43], that is

$$\overline{\lambda}\,\boldsymbol{u}^\dagger + (\nabla\boldsymbol{U})^\mathrm{T}\,\boldsymbol{u}^\dagger - (\nabla\boldsymbol{u}^\dagger)\,\boldsymbol{U} - \nabla\cdot\boldsymbol{\sigma}(\boldsymbol{u}^\dagger, p^\dagger) = 0 \qquad \text{in } \Omega_\mathrm{f}, \tag{20}$$

$$-\nabla\cdot\boldsymbol{u}^\dagger = 0 \qquad \text{in } \Omega_\mathrm{f}, \tag{21}$$

$$-\boldsymbol{u}^\dagger = \mathbf{0} \qquad \text{on } \Gamma_\mathrm{rgd}. \tag{22}$$

Advection terms induce non-normality in the system: unlike the solid equations, the adjoint fluid equations do not coincide with the direct ones. On the other hand, very non-standard terms are found in the coupling terms. The adjoint extension equation writes as follows:

$$\nabla\boldsymbol{U}^\mathrm{T}\Big(\overline{\lambda}\,\boldsymbol{u}^\dagger + (\nabla\boldsymbol{U})^\mathrm{T}\boldsymbol{u}^\dagger - (\nabla\boldsymbol{u}^\dagger)\boldsymbol{U}\Big) + (\nabla\boldsymbol{u}^\dagger)^\mathrm{T}\nabla\boldsymbol{U}\,\boldsymbol{U} + \nabla\cdot\Big(\nabla\boldsymbol{\xi}_e^\dagger + \boldsymbol{\Sigma}_\mathrm{e}^\dagger(\boldsymbol{U}, P, \boldsymbol{u}^\dagger, p^\dagger)\Big) = 0 \quad \text{in } \Omega_\mathrm{e}. \tag{23}$$

$$-\boldsymbol{\xi}_e^\dagger = \mathbf{0} \quad \text{on } \partial\Omega_\mathrm{e}, \tag{24}$$

where $\boldsymbol{\xi}_e^\dagger$ only appears through the Laplace extension operator $\nabla\cdot(\nabla\boldsymbol{\xi}_e^\dagger)$. In the above equation, we have also introduced a tensor $\boldsymbol{\Sigma}_{\mathrm{e}}^\dagger(\boldsymbol{U},P,\boldsymbol{u}^\dagger,p^\dagger)$ that takes the following expression,

$$\boldsymbol{\Sigma}^\dagger(\boldsymbol{U},P,\boldsymbol{u}^\dagger,p^\dagger)=\frac{2}{\mathcal{R}_{\mathrm{e}}}\left\{\Big(\mathbf{D}(\boldsymbol{U}):\mathbf{D}(\boldsymbol{u}^\dagger)\Big)\mathbf{I}-\Big((\nabla\boldsymbol{u}^\dagger)^{\mathrm{T}}\mathbf{D}(\boldsymbol{U})+(\nabla\boldsymbol{U})^{\mathrm{T}}\mathbf{D}(\boldsymbol{u}^\dagger)\Big)\right\}-P\,\boldsymbol{\Phi}'(\boldsymbol{u}^\dagger)^{\mathrm{T}}-P^\dagger\boldsymbol{\Phi}'(\boldsymbol{U})^{\mathrm{T}}. \tag{25}$$

In (24) the adjoint displacement $\boldsymbol{\xi}_e^\dagger$ is prescribed to be zero at the fluid-solid interface. This makes sense: adjoints can indeed be interpreted as the receptivity to forcings of the direct equations [42]; with this respect the adjoint displacement expresses the receptivity to a forcing of the extension equation, that must be zero on the fluid-solid interface: otherwise, this would signify that the extension equation may influence the physical problem. Finally, adjoint velocity and stress conditions are prescribed on the fluid-solid interface as follows:

$$\boldsymbol{u}_s^\dagger-\boldsymbol{u}^\dagger=\mathbf{0} \qquad \text{on } \Gamma, \tag{26}$$

$$\overline{\lambda}\,\boldsymbol{\sigma}(\boldsymbol{u}^\dagger,p^\dagger)\boldsymbol{n}+\Big(\nabla\boldsymbol{\xi}_e^\dagger+\boldsymbol{\Sigma}_{\mathrm{e}}^\dagger(\boldsymbol{U},P,\boldsymbol{u}^\dagger,p^\dagger)\Big)\boldsymbol{n}=\boldsymbol{\sigma}_{\mathrm{s}}(\boldsymbol{u}_s^\dagger)\boldsymbol{n} \qquad \text{on } \Gamma. \tag{27}$$

Since the adjoint velocities express physically the receptivity to a physical mechanism that would have injected momentum in the system [44], they should be continuous across the fluid-solid interface, as prescribed by (26). The adjoint interace stress condition (27) takes an highly non-trivial form [details]. Finally, the other boundary conditions are the zero solid displacement $\boldsymbol{\xi}^\dagger=\mathbf{0}$ on $\partial\Omega_{\mathrm{s}}\setminus\Gamma$, and the outflow condition $\boldsymbol{\sigma}(\boldsymbol{u}^\dagger,p^\dagger)\boldsymbol{n}+(\boldsymbol{U}\cdot\boldsymbol{n})\boldsymbol{u}^\dagger=\mathbf{0}$ on Γ_{out}. The velocity is prescribed to be zero on Γ_{in} and Γ, while $\boldsymbol{u}^\circ\cdot\boldsymbol{n}=0$ on Γ_{lat}.

2.3.2. Adjoint stationary equation

When there is no steady deformation, the adjoint steady equation reduces to the adjoint Navier-Stokes equations, forced by sensitivities $\nabla_{\boldsymbol{U}}(\lambda)$ and $\nabla_P(\lambda)$. All computations done, we obtain

$$\begin{aligned}\nabla_{\boldsymbol{U}}(\lambda)=&-(\overline{\nabla\boldsymbol{u}^\circ})^{\mathrm{T}}\boldsymbol{u}^\dagger+\nabla\boldsymbol{u}^\dagger\overline{\boldsymbol{u}^\circ}\\&-\boldsymbol{\Phi}'(\overline{\boldsymbol{\xi}_e^\circ})^{\mathrm{T}}\nabla\boldsymbol{U}^{\mathrm{T}}\,\boldsymbol{u}^\dagger+\nabla\boldsymbol{u}^\dagger\boldsymbol{\Phi}'(\overline{\boldsymbol{\xi}_e^\circ})\boldsymbol{U}\\&-\overline{\lambda}\left(\nabla\boldsymbol{u}^\dagger\,\overline{\boldsymbol{\xi}_e^\circ}+\nabla\cdot\overline{\boldsymbol{\xi}_e^\circ}\,\boldsymbol{u}^\dagger\right)\\&+\nabla\cdot\boldsymbol{\Sigma}'(\boldsymbol{u}^\dagger,p^\dagger;\overline{\boldsymbol{\xi}_e^\circ})\end{aligned} \tag{28}$$

for the sensitivity to variations of the steady flow. The first line is exactly that obtained by [37], while the other terms represent the corrections coming from dynamic flexibility effects. In the fluid-elastic case, there is furthermore a sensitivity to pressure variations,

$$\nabla_P(\lambda)=\boldsymbol{\Phi}'(\overline{\boldsymbol{\xi}_e^\circ})^{\mathrm{T}}:\nabla\boldsymbol{u}^\dagger. \tag{29}$$

The adjoint stationary equation write as follows:

$$\begin{aligned}(\nabla\boldsymbol{U})^{\mathrm{T}}\,\boldsymbol{U}^\dagger-(\nabla\boldsymbol{U}^\dagger)\,\boldsymbol{U}-\nabla\cdot\boldsymbol{\sigma}(\boldsymbol{U}^\dagger,P^\dagger)&=\nabla_{\boldsymbol{U}}(\lambda) &&\text{in } \Omega_{\mathrm{f}},\\ -\nabla\cdot\boldsymbol{U}^\dagger&=\nabla_P(\lambda) &&\text{in } \Omega_{\mathrm{f}},\\ -\boldsymbol{U}^\dagger&=\mathbf{0} &&\text{on } \Gamma\cup\Gamma_{\mathrm{rgd}},\end{aligned} \tag{30}$$

completed by the outflow condition $(\boldsymbol{U}\cdot\boldsymbol{n}_{\mathrm{f}})\boldsymbol{U}^\dagger+\boldsymbol{\sigma}(\boldsymbol{U}^\dagger,P^\dagger)\boldsymbol{n}_{\mathrm{f}}-\boldsymbol{\sigma}^\dagger(\boldsymbol{u}^\dagger,p^\dagger,\boldsymbol{\xi}_e^\circ)\boldsymbol{n}=\mathbf{0}$ on Γ_{out} and the other farfield velocity conditions.

2.4. Fluid-elastic shape optimization and numerical implementation

2.4.1. Shape optimization cost-function

For practical applications, we introduce a real cost-function based on the most unstable linear mode eigenvalue of the eigenvalue problem, and consider the shape optimization problem

$$\min_{\Omega\in\mathcal{W}_{\mathrm{ad}}}\mathscr{J}(\Omega),\qquad \mathscr{J}(\Omega)=\frac{\alpha_r}{2}\Big(\lambda^r(\Omega)-\lambda_c^r\Big)^2+\frac{\alpha_i}{2}\Big(\lambda^i(\Omega)-\lambda_c^i\Big)^2, \tag{31}$$

again under the constraints of the steady Navier-Stokes flow and the linear perturbation problem. In the above notation, λ_c^r and λ_c^i are the control parameters, and α_r and α_i belong to $\{0,1\}$. For instance when $\alpha_r = 1$ and $\alpha_i = 0$ one tries to control only the growth-rate of the perturbations while the frequency is left free. The (real) gradient with respect to the (real-valued) cost-function (31) is deduced from the (complex) shape sensitivity G_λ given in (16)–(17) as

$$G = \alpha_r(\lambda^r - \lambda_c^r)\,\mathfrak{Re}\big\{G_\lambda\big\} + \alpha_i(\lambda^i - \lambda_c^i)\,\mathfrak{Im}\big\{G_\lambda\big\}. \tag{32}$$

2.4.2. Extended-regularized gradient

Once the shape derivative is computed from (16) and (17), the shape gradient is obtained by identifying the integral in (16) with the appropriate scalar product. The most straightforward choice consists in choosing the standard $\mathcal{L}^2$ scalar product on $\Gamma_{\rm rgd}$, i.e.

$$\lambda'(\Gamma_{\rm rgd})(\boldsymbol{\theta}) = \langle \mathbf{G}_\lambda, \boldsymbol{\theta}\rangle_{\mathcal{L}^2(\Gamma_{\rm rgd})} \quad \forall\, \boldsymbol{\theta} \in \Theta \qquad \Rightarrow \qquad \boldsymbol{G}_\lambda = G_\lambda\, \boldsymbol{n} \ \text{ on } \ \Gamma_{\rm rgd}. \tag{33}$$

An other choice, similar in principle, is made practically. Choosing the $\mathcal{L}^2$ scalar product comes indeed with a numerical difficulty: the gradient is defined only at the fluid-structure interface, that is practically a boundary of the fluid mesh. Using the gradient information to deform the surface vertices is thus likely to result in degenerated cells in the neighbouring if the update step is too large. For these reasons, the interface gradient information is propagated onto the whole domain using the so-called $\mathcal{H}^1$-method [45, 46], that also increases the smoothness of the gradient. This method simply consists in identifying the shape gradient by means of the $\mathcal{H}^1$ scalar product on $\Omega_{\rm f}$ defined by $\langle \boldsymbol{a}, \boldsymbol{b}\rangle_{\mathcal{H}^1(\Omega_{\rm f})} = \int_{\Omega_{\rm f}} (\boldsymbol{a}\cdot\boldsymbol{b} + \nabla\boldsymbol{a} : \nabla\boldsymbol{b}) \mathrm{d}\Omega$. This defines a variational formulation for a Poisson equation

$$\lambda'(\Gamma_{\rm rgd})(\boldsymbol{\theta}) = \big\langle \mathbf{G}_\lambda, \boldsymbol{\theta}\big\rangle_{\mathcal{H}^1(\Omega)} \quad \forall\, \boldsymbol{\theta} \in \Theta \qquad \Rightarrow \qquad \begin{cases} \nabla^2 \mathbf{G}_\lambda - \mathbf{G}_\lambda = \mathbf{0} & \text{in} \quad \Omega_{\rm f}, \\ (\nabla \mathbf{G}_\lambda)\boldsymbol{n} = G_\lambda\, \boldsymbol{n} & \text{on} \quad \Gamma_{\rm rgd}, \\ \mathbf{G}_\lambda = \mathbf{0} & \text{on} \quad \partial\Omega_{\rm f} \setminus \Gamma_{\rm rgd}. \end{cases} \tag{34}$$

In all what follows, the gradients will be computed from (34). In that case, one obtains a deformation field that extends over the whole domain $\Omega_{\rm f}$, while the deformation along the interface $\Gamma_{\rm rgd}$ is not necessarily aligned with the normals.

Note that with the $\mathcal{H}^1$-based approach, the deformation field has no longer components only along the normals at the deformable edges. To address mesh-related issues, once the regularized gradient is computed and the new position of the interface is determined, the region around the optimization interface is remeshed, so as to prevent from mesh cells degeneracy.

2.4.3. Numerical algorithm

The optimization loop is represented schematically on the Fig. 3. The procedure only requires an initial shape $\Omega^{(0)}$ as an input, which is that with the circular cylinder. Within one iteration of the algorithm, several steps are realized sequentially. First, the non-linear stationary problem [REF] is solved. The steady deformed configuration is then computed, and the direct eigenvalue problem [REF] is assembled, then solved. The adjoint eigenvalue problem [REF] is solved using the discrete transpose-conjugate approach, which avoids having to reassemble the corresponding matrix. The direct and adjoint modes are scaled according to [REF] and [REF]. Then, the adjoint stationary equation [REF] is solved. The matrix for this problem is also obtained practically by taking the transpose of the Jacobian matrix used in the Newton loop considered for solving [REF]. Finally, the shape gradient is computed using the formula (32). All matrices are assembled within the software FreeFEM [47]. The sparse, direct LU solver Mumps [48] is used for all matrix inversions, while the library Arpack [49] is called for eigenvalue computations.

A fixed descent step k is chosen, that sets the magnitude of the shape deformations for the current iteration. The extended-regularized descent direction is computed from (**??**), and the mesh is updated accordingly. The stop criterion is set on the magnitude of the deformation of this deformation field. Finally, the non-linear solution at the current step is interpolated on the new mesh and serves as an initial guess for the next step.

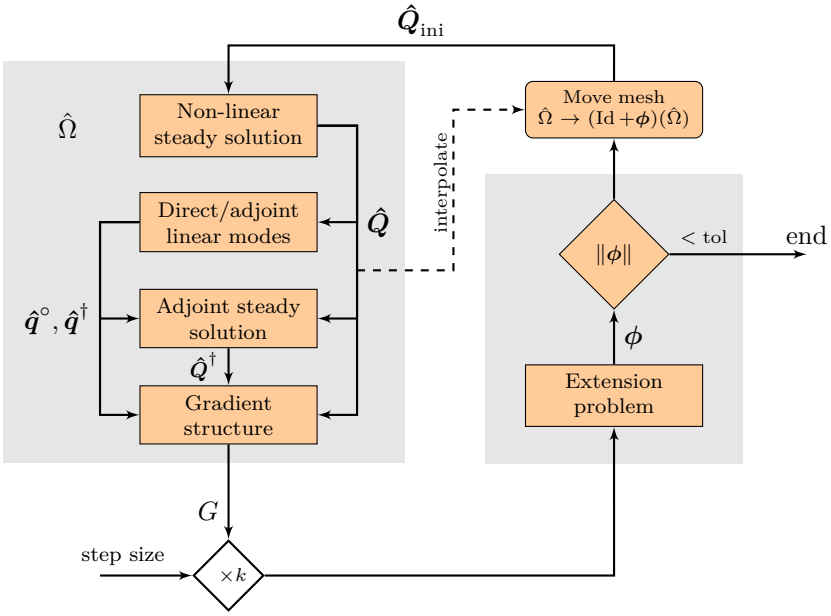

Figure 3: Shape optimization loop.

3. Results

In the following, we first describe the fluid-solid mode found at the Reynolds number of $\mathcal{R}_e = 80$ and a stiffness parameter of $\mathcal{E}_s = 105000$. The general shape sensitivities are then introduced and discussed. Results of shape optimization for stabilizing the modes are presented. Finally, we consider a case where one tries to design an unstable configuration oscillating at a prescribed frequency.

3.1. Description of the unstable mode

Solving the stationary flow equation over the rigid geometry results in the steady flow represented in the upper right picture in Fig. 4. We observe that the flow detaches from the cylinder, resulting in a recirculation region that extends down to $x = 4.32$. The associated fluid-elastic spectrum computed from the fluid-solid eigenvalue problem is represented in the graph on the left side and shows one unstable eigenvalue pair $\lambda_{(S)} = 2.07 \times 10^{-2} \pm 0.97\mathbf{i}$. A representation of the real part of the streamwise velocity component of the mode is also shown in the bottom right picture, showing a typical vortex shedding pattern in the wake, associated to a bending vibration mode in the solid.

3.2. Shape gradients

Let us first turn our attention to deformations of the cylinder's surface that modify the unstable mode along the real and imaginary parts of the shape gradient. The shape gradients are reported in Fig. 5. On top, the deformations producing the greatest drift of the growth-rate (i.e. $\mathfrak{Re}\{\mathbf{G}_\lambda\}$) are reported, while the deformations modifying the frequency ($\mathfrak{Im}\{\mathbf{G}_\lambda\}$) are reported at the bottom. The three graphs on the left side present the interface deformation obtained with the $\mathcal{H}^1$ method (the deformation field in the domain is not represented for readability reasons), decomposed between the steady $\mathbf{G}_{\lambda,s}$ and unsteady $\mathbf{G}_{\lambda,u}$ components. The graph on the right side displays the evolution of G_λ with θ the local position along the cylinder's interface. Although less visual than the representation of the deformation *vector* field $\mathbf{G}_\lambda$, the *scalar* field G_λ makes it easier to compare the different gradients.

Focusing first on the real part, it is observed that both the steady and the unsteady components have roughly the same amplitude, and act in an opposed way. The stationary component is associated with a crushing in the directions $\theta \pm 135°$, while the unsteady component prescribes a blowing of the shape along the vertical axis. If the slendering of the shape, by reduction of the cross-section, has an evident

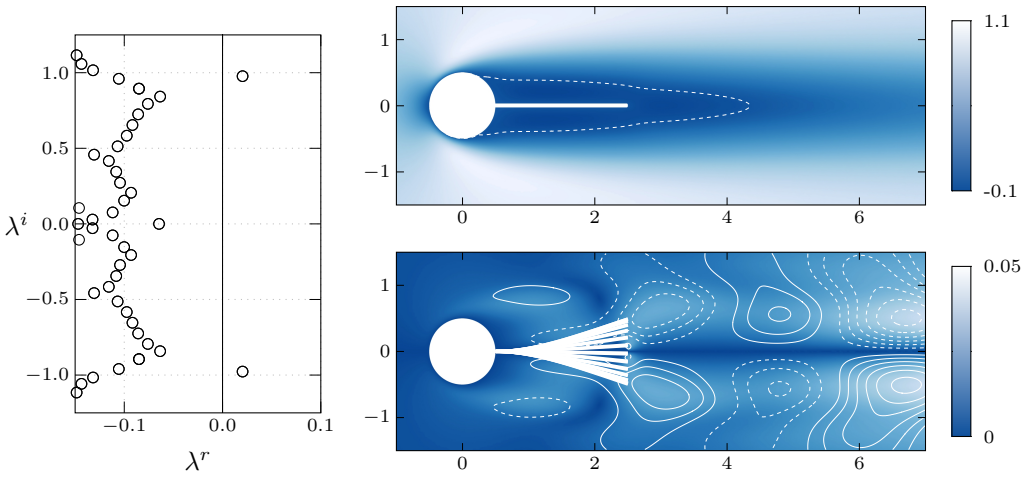

Figure 4: Reference cases (S) before shape optimization. Top right: streamwise velocity component of the stationary flow, limits of the backflow region emphasized by the dashed line. Left: eigenvalue spectrum. Bottom right: modulus (colors) and real part (contours in the range ± 0.05 by steps 0.01, dashed negative) of the leading mode streamwise velocity component, and superposition of snapshots of the solid deformation at different phases.

stabilizing effect, the blowing effect observed in $\boldsymbol{\phi}_s$ is less evident to interpret. The combination of the two seems to generate a more "C-shaped" bluff-body when it comes to increase the growth-rate of the mode. The imaginary parts of the components of the gradient (associated to a modification of the frequency) have roughly the same signs than the real parts, but with very different amplitudes. The amplitude for the steady component is actually about 10 times higher than the amplitude of the unsteady component. For instance, increasing infinitesimally the frequency of the mode therefore essentially requires to deform the shape into an ellipse whose major axis is directed along the horizontal axis.

Let us also evaluate the evolution of the eigenvalue in the complex plate when the shape is modified according to the real or imaginary parts of the gradient. The linear evolution in the vicinity of the initial eigenvalue can be evaluated using (16). For the case of a deformation according to $\mathfrak{Re}(\mathbf{G}_\lambda)$, taking $\boldsymbol{\theta} = t\,\mathfrak{Re}\{G_\lambda\}\boldsymbol{n}$ for $t \in \mathbb{R}$ gives

$$\lambda(t) = \lambda(0) + t \int_{\Gamma_{\text{rgd}}} G_\lambda\, \mathfrak{Re}\{G_\lambda\} \mathrm{d}\Gamma + \circ(t)$$

where t is a parameter for the magnitude of the deformation. At the leading order, eliminating the parameter t gives

$$\lambda^r(t) - \lambda^r(0) = \frac{\int_{\Gamma_{\text{rgd}}} \mathfrak{Re}\{G_\lambda\}^2 \mathrm{d}\Gamma}{\int_{\Gamma_{\text{rgd}}} \mathfrak{Re}\{G_\lambda\}\mathfrak{Im}\{G_\lambda\} \mathrm{d}\Gamma} \big(\lambda^i(t) - \lambda^i(0)\big). \tag{35}$$

Similarly, for the case of a deformation according to $\mathfrak{Im}(\mathbf{G}_\lambda)$, taking $\boldsymbol{\theta} = t\,\mathfrak{Im}\{G_\lambda\}\boldsymbol{n}$ for $t \in \mathbb{R}$ gives, from (16), the equation

$$\lambda^r(t) - \lambda^r(0) = \frac{\int_{\Gamma_{\text{rgd}}} \mathfrak{Re}\{G_\lambda\}\mathfrak{Im}\{G_\lambda\} \mathrm{d}\Gamma}{\int_{\Gamma_{\text{rgd}}} \mathfrak{Im}\{G_\lambda\}^2 \mathrm{d}\Gamma} \big(\lambda^i(t) - \lambda^i(0)\big). \tag{36}$$

Straight lines corresponding to (35) (dashed red) and (36) (dashed green) are reported in Fig. 6 [commentaire].

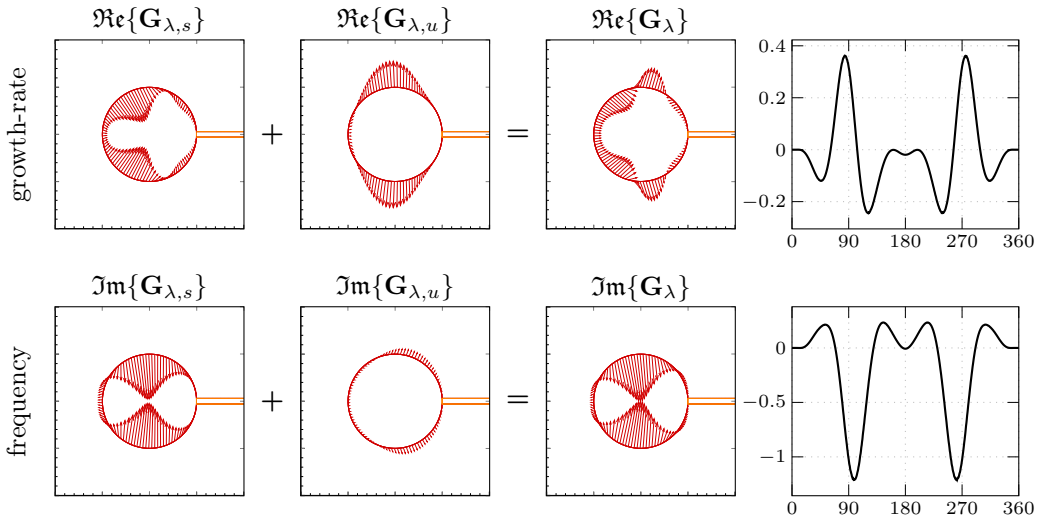

Figure 5: Gradients for the mode (S)

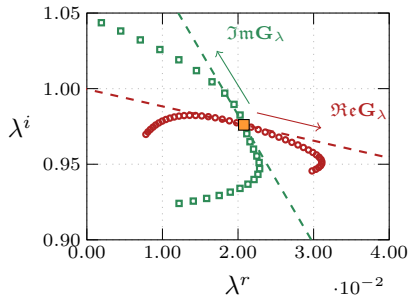

Figure 6: Evolution in the complex plane of the leading eigenvalue obtained by repeating the full fluid-solid stability analysis after a modification of the shape according to $\mathfrak{Re}\{\mathbf{G}_{\lambda}\}$ (red) and $\mathfrak{Im}\{\mathbf{G}_{\lambda}\}$ (green). The straight dashed line represent the prediction of the sensitivity analysis (Eqns. (35) and (36)).

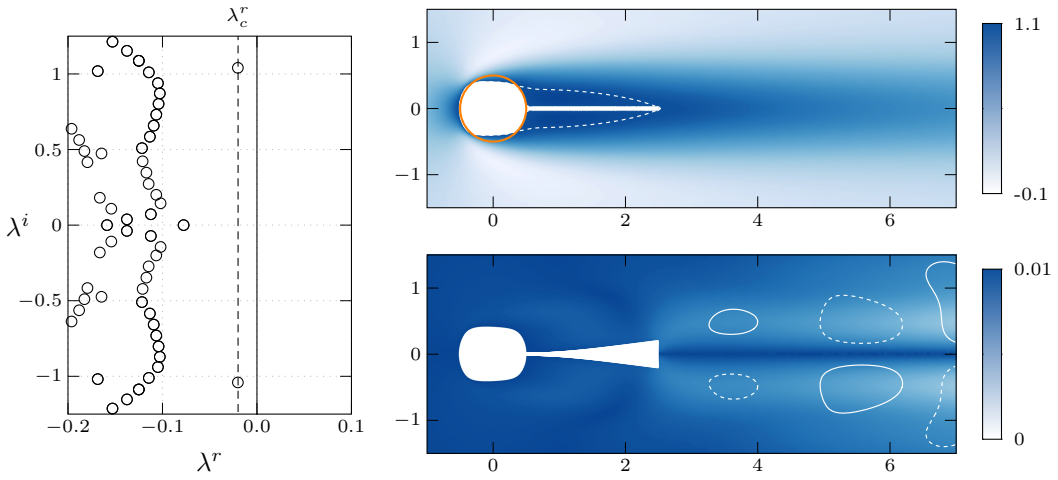

Figure 7: Stabilizing shapes. Top right for both cases: streamwise velocity component of the stationary flow, limits of the backflow region emphasized by the dashed line. Left: eigenvalue spectrum. Bottom right: modulus (colors) and real part (same contours as in Fig. 4) of the leading mode streamwise velocity component, and superposition of snapshots of the solid deformation at different phases.

4. Fluid-elastic shape optimization

4.1. Shape optimization for stabilizing the modes

We focus in this section on the shape optimization for controlling the growth-rate of the modes. We therefore consider $\alpha_r = 1$ and $\alpha_i = 0$, i.e. in this section the cost-function writes as

$$\mathscr{J}(\hat{\Omega}) = \frac{1}{2}\left(\lambda^r(\hat{\Omega}) - \lambda_c^r\right)^2.$$

Using the gradient descent algorithm described above, optimal shapes satisfying $\lambda^r = \lambda_c^r$ (up to a prescribed tolerance set on the value of the cost-function) might be eventually computed. In particular, setting $\lambda_c^r < 0$ amounts to finding shapes that kill the instability. On the other hand, the frequency is left unconstrained in this case. We first set the growth-rate control to a slightly negative value $\lambda_c^r = -0.02$. For both type of modes, less than ten iterations are needed for the cost-function to reach a plateau at 10^{-8}.

The results are reported in Fig. 7. The optimal shape that stabilizes the mode has a reduced cross-section. This has obviously a stabilizing effect, since it reduces the apparent Reynolds number. The recirculation region is much smaller in the optimized case (limit at $x = 4.35$ in the initial case and $x = 2.81$ in the optimized case) and touches the tip of the plate.

Let us now vary the value of the target growth-rate λ_c^r. The least stable eigenvalue obtained once the optimization has converged is represented in the complex plane in the Fig. 8. The vertical axis thus displays the reached growth-rate λ^r as well as the objective growth-rate λ_c^r, which are the same up to the prescribed tolerance. The initial (non-optimized) eigenvalue is depicted with the ■ symbol. A global trend is observed: the more stable the optimized mode, the higher the frequency. On the other hand, when the target growth-rate is set to positive values, the frequency reach a maxima as λ_c^r is increased up to about 0.05, then decreases again. A few shapes are represented in the inserts (arrows indicating which is the corresponding eigenvalue).

4.2. Shape optimization for controlling the frequency of the modes

We now consider the case where the frequency is set to a specified value λ_c^i, while the growth-rate is left free to evolve. In the present case, the cost-function therefore writes as

$$\mathscr{J}(\hat{\Omega}) = \frac{1}{2}\left(\lambda^i(\hat{\Omega}) - \lambda_c^i\right)^2.$$

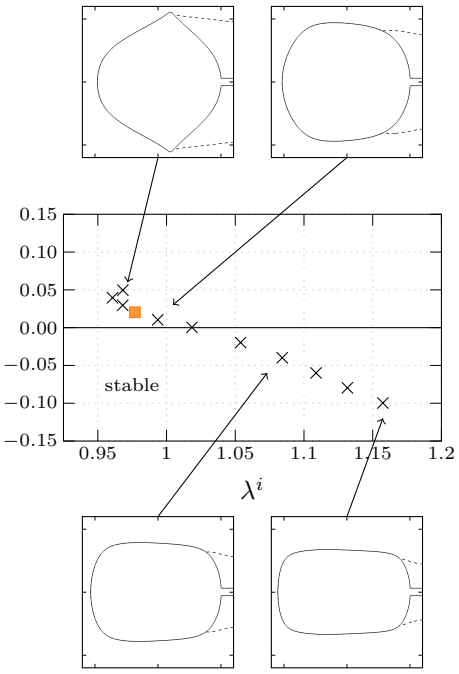

Figure 8: Shape optimization for controlling the growth-rate. Representation, after shape optimization, of the leading coupled fluid-structure eigenvalues for the case where the growth-rate is optimized (the growth-rate satisfies at convergence $|\lambda^r - \lambda_c^r| < \text{tol}$). The square symbols represent the initial location in the spectrum of the leading eigenvalue. A few optimized shapes are indicated with the inserts, where the limits of the back-flow region behind the bluff-body has been marked with a dashed line.

The obtained eigenvalues at convergence of the algorithm are reported in the Fig. 9 for both reference cases, as a function of the target frequency λ_c^i. We observe that the converged eigenvalue are clustered in the same region of the complex plane as previously: for comparison, the gray crosses represents the location of the optimized eigenvalues obtained by targeting a specified growth-rate. It seems that the optimizations with $(\alpha_r, \alpha_i) = (1, 0)$ and $(\alpha_r, \alpha_i) = (0, 1)$ thus result in modes that roughly follow the same tendency, i.e. the higher the frequency, the more stabilized is the mode.

Note that in the case of a stable flow, changing the target frequency or growth-rate would result in stable flows having different features (drag/lift) depending on the choice of λ_c^i, but there is *a priori* no simple way to connect the objective eigenvalue to integrated quantities such as the drag of the object in the steady flow. In this case, it is more adapted to adopt an approach in which the objective-function is directly the drag like for instance in the work by [6], or a measure of the distance to a prescribed velcity er energy criteria [50]. This can be relatively easily done within the present framework — the derivation of the shape gradient is in that case by any means simpler as what is needed in the unsteady case. In the next section, we therefore perform a combined optimization aiming at specifying both the frequency *and* the growth-rate.

4.3. Combined frequency & growth-rate optimization: design of a fluid-structure oscillator

A practical outcome for the frequency-based optimization would be the ability to design kind of a fluid-structure oscillator, beating at a prescribed frequency. In the case where the flow is slightly unstable, an exponential growth of perturbations oscillating at frequency λ_c^i will be observed (in an experiment or in non-linear simulations) in the linear regime of development of the instabilities if no significant transient growth affects the process [51]. Hopefully, some features observed linearly would then persist once the non-linear limit-cycle is reached, as it was already observed in the previous chapter. This is all the most likely to happen when the amplitude of the perturbations is low [34]. If all these requirements are fulfilled, the optimized system would behave as a self-sustained oscillator at a frequency close to λ_c^i. Practically,

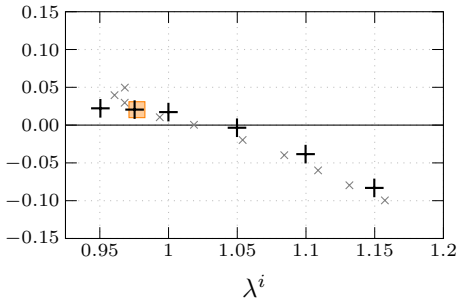

Figure 9: Shape optimization for controlling the frequency. Representation, after shape optimization, of the leading coupled fluid-structure eigenvalues (+) for the case where the frequency is optimized (the frequency satisfies at convergence $|\lambda^i - \lambda_c^i| <$ tol). The square symbols represent the initial location in the spectrum of the leading eigenvalue. For the sake of comparison, the eigenvalues reported in the Fig. 8 (optimization of the growth-rate only) are also reported (x).

these features could for instance be exploited to design more efficient energy-harvesting devices, by tuning the resonance frequencies of the system in order to maximize the energy transfer [52].

To do so, the growth-rate should nevertheless stay positive. The approach where only the frequency is taken as a part of the cost-function is thus not very appropriate, since we have seen above that in that case the flow becomes at some point *stable* when the frequency target is increased. We therefore set here a cost-function that depends on both the growth-rate and the frequency, that is,

$$\mathscr{J}(\hat{\Omega}) = \frac{1}{2}\left(\lambda^r(\hat{\Omega}) - \lambda_c^r\right)^2 + \frac{1}{2}\left(\lambda^i(\hat{\Omega}) - \lambda_c^i\right)^2.$$

On the contrary to the previous case where an high target frequency results in a stable flow, an unstable fluid-structure oscillator at a prescribed frequency can be designed here. In the following, we choose a constant positive growth-rate $\lambda_c^r = 0.01$ for all cases.

An overview of the optimization results is displayed in the Fig. 11., which is indicated by the dashed line in the figure. As the frequency objective is varied, different shapes are obtained, four of them being displayed in the inserts (top left: $\lambda_c^i = 0.925$, top right: $\lambda_c^i = 0.950$, bottom left: $\lambda_c^i = 1.025$, bottom right: $\lambda_c^i = 1.1$). For the case with $\lambda_c^i = 0.925$, a second unstable mode located at $0.0411 \pm 0.514\mathbf{i}$ is found in the spectrum of the linearised problem, after convergence of the algorithm, in addition to the controlled mode located at $0.01 \pm 0.925\mathbf{i}$. Since its growth-rate is much larger than the target value of $\lambda_c^r = 0.01$, it overcomes the growth of the optimized mode and is the predominant mode of the flow. A two-points optimization taking into account of these two unstable modes would be mandatory to treat this specific case, but will not be considered here (although technically feasible). For all the other cases displayed in the Fig. 11, only one unstable mode is found.

Let us describe more precisely the obtained flow for three cases, also represented in the inserts in the Fig. 11. The corresponding results are reported in the Fig. 10 where, for sake of comparison, the initial (i.e. before the optimization process) shape is materialized by the orange circle, and the limit of the recirculating region of the stationary flow along the streamwise axis is marked with a cross. The cases with $\lambda_c^i = 0.95$ (top), $\lambda_c^i = 1.025$ (middle) and $\lambda_c^i = 1.1$ (bottom) are represented. First, we note that even if the three modes have the same growth-rate, they are associated to steady flows having recirculating regions (whose limits are marked with the dashed line) of very different lengths: the maximal extension is reached at $x = 5.39$ for the lowest-frequency case (a), $x = 3.23$ for case (b) and $x = 2.65$ for the higher-frequency case (c). This situation is quite different from what is observed for a rigid case. In the circular cylinder flow for instance, the growth-rate of unstable modes is found to increase with the length of the stationary back-flow region [44]. Here, the shorter the recirculating region, the higher the frequency. A possible mechanism to explain this behaviour is that the ratio between the recirculating region and the splitter plate length might determine the vibration frequency, by specifying at which point vortices should be released so as to interact favourably with the solid. In this sense in (a) the vortex formation region is larger as in the case (c), and this increased half-width makes it longer for a vortex to complete

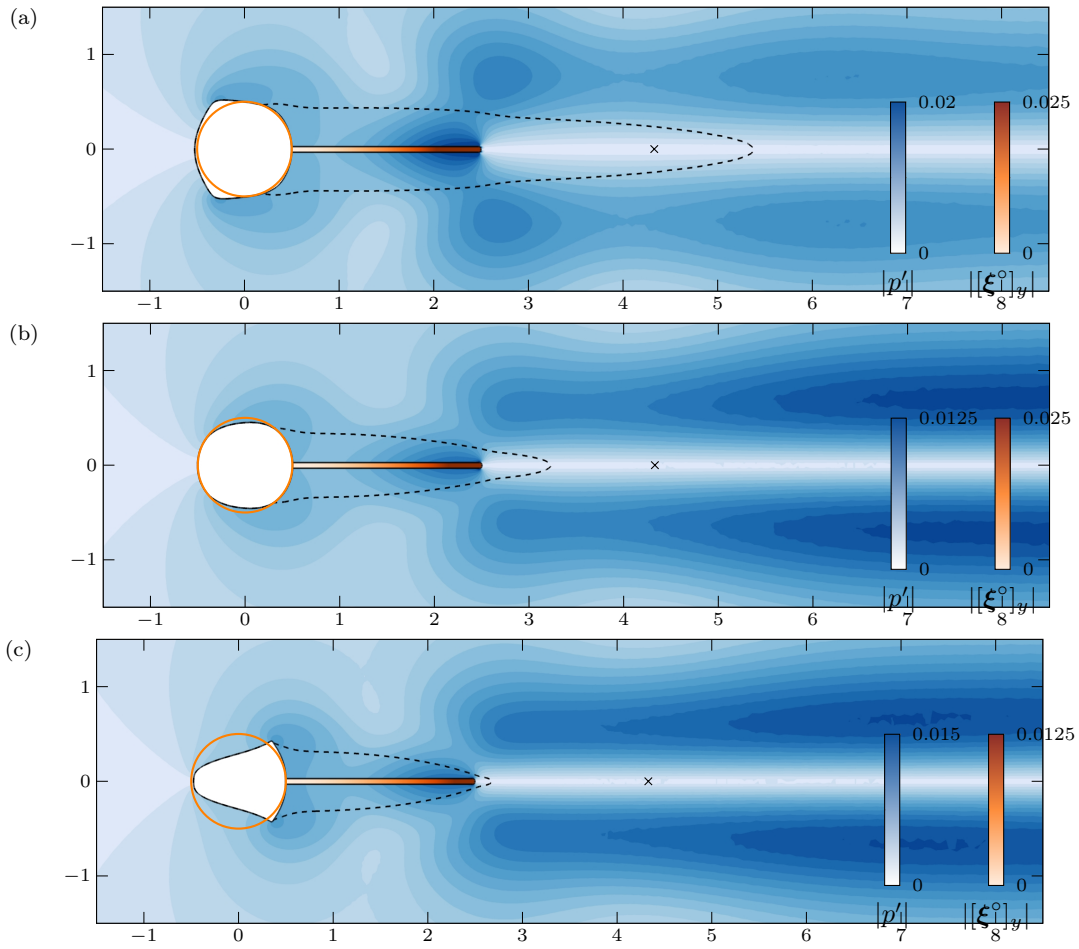

Figure 10: Optimal fluid-structure oscillators. For the cases with $\lambda_c^r = 0.01$ and (a) $\lambda_c^i = 0.95$, (b) $\lambda_c^i = 1.025$ and (c) $\lambda_c^i = 1.1$, plot of the absolute value of the Eulerian pressure perturbation $p' - p' - \nabla P\, \boldsymbol{\xi}'_e$ (blue colors in the fluid) and of the absolute value of the solid deformation mode , transverse component (orange color in the solid). The limits of the back-flow region of the steady flow is marked with the dashed black line, while the maximal x extension of the back-flow region for the *initial, non-optimized shape* materialized with the orange circle is marked with a cross ($\times$).

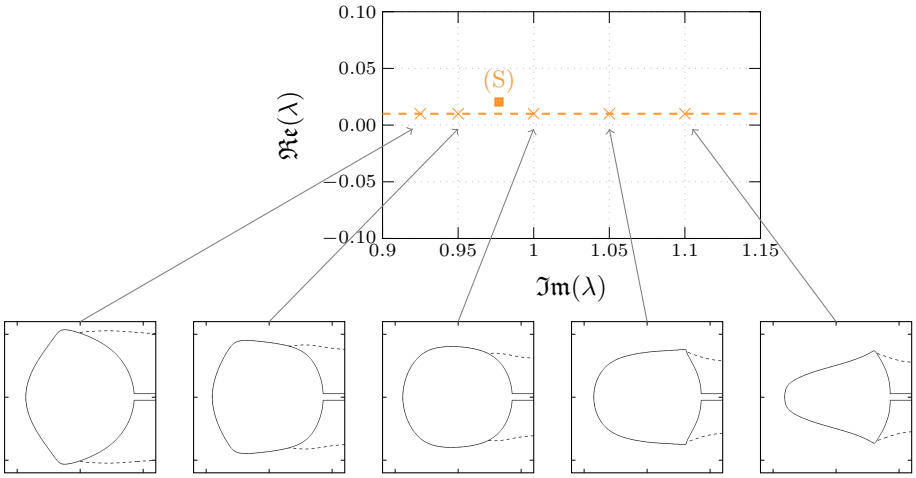

Figure 11: Shape optimization for designing a fluid-structure oscillator. Plot, in the (λ^i, λ^r) plane, of the converged eigenvalues obtained with an optimization for the growth-rate (fixed to $\lambda_c^r = 0.01$) nd the frequency (variing between 0.925 and 1.1). A few optimal shapes are represented, with $\lambda_c^i = 0.925$ (upper left), $\lambda_c^i = 0.95$ (upper right), $\lambda_c^i = 1.05$ (below left) and $\lambda_c^i = -1.1$ (below right). The eigenvalue corresponding to the initial shape (circular cylinder) is represented with the orange square symbol.

its period of oscillation. Note however that previous studies, in which the length of a flexible splitter attached behind a circular [53, 54] or square [55] cylinder was varied, reported that the vortex shedding frequency possible varies non-monotonously, and in any case non-linearly with the length of the splitter plate. Complex mechanisms might therefore be at play.

The pressure mode in the fluid region is depicted with a blue color. The absolute value is represented so as to have a visualisation independent from the phase (real and imaginary parts are symmetric with respect to the axis $y = 0$). The structures close the the solid have roughly the same shape for all cases, indicating that the fluid-structure dynamics close to the solid is not dramatically different between the three cases. In particular, the absolute transverse displacement in the solid indicates that the vibration pattern in the solid is in all cases that of a bending mode with one vibration node at the clamped end.

Finally, the non-linear behaviour of the fluid-structure oscillators can also investigated. How does the "optimal" linear frequency obtained with the time-linearised shape optimization process relates to the non-linear frequency resulting from a fully non-linear, time-marching simulation ? Except for the case $\lambda_c^i = 0.925$, that comes with another unstable mode (the corresponding non-linear simulation comes with an oscillation frequency of $\omega_{\text{DNS}} = 0.69$), a fairly good agreement is found. For instance, for the case $\lambda_c^i = 1$, the non-linear frequency obtained using a Fast Fourier Transform of the lift signal once the limit cycle has been reached is $\omega_{\text{DNS}} = 1.037$. This is in accordance with the observations in the previous chapter, where we observed that the predictions for the linear frequency are found to match pretty well with that extracted from the non-linear limit-cycles. The time-series exhibits a symmetric flapping regime with an amplitude of oscillation of the tip of the plate of 0.12.

5. Conclusion

Appendix A. Derivation of the formula for the shape gradient

In this section, details are given on the derivation of the shape gradient formula (17) and of the adjoint equations. Following Céa [40], we rely here on a Lagrangian approach, associated to a Lagrangian parametrization of the deformations (through shape optimization) of the domain.

Appendix A.1. Lagrangian formulation

When using the Lagrangian approach [40] for performing a shape sensitivity analysis, care has to be taken when it comes to the definition of the spaces where the different variables live in. Since $\Omega_{\text{f}} = \Omega_{\text{f}}(\boldsymbol{\theta})$

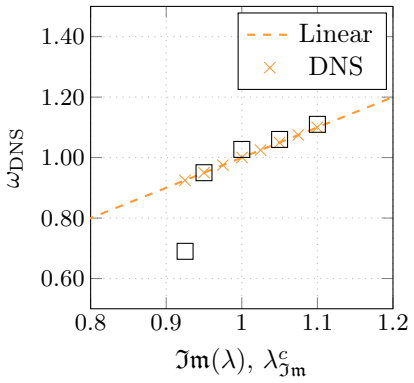

Figure 12: Comparison with non-linear simulations

and $\boldsymbol{\theta}$ is itself an unknown of the problem, variables for the fluid problem should be defined on spaces that are *independent* of Ω_{f}, otherwise the Lagrangian function associated to the problem would not involve independent variables. For that reason, Dirichlet boundary conditions on Γ_{rgd} are enforced using a Lagrange multiplier. Fluid-solid velocity and displacement interface conditions on Γ are also enforced using Lagrange multipliers. The following spaces are introduced,

$$\mathcal{U}^f = \Big\{ \boldsymbol{f} \in \mathcal{H}^1(\mathbb{R}^d),\, \boldsymbol{f}|_{\Gamma_{\mathrm{in}}} = \boldsymbol{u}_\infty,\, \boldsymbol{f}\cdot\boldsymbol{n}|_{\Gamma_{\mathrm{lat}}} = 0 \Big\}, \quad \mathcal{U}^f_0 = \Big\{ \boldsymbol{f} \in \mathcal{H}^1(\mathbb{R}^d),\, \boldsymbol{f}|_{\Gamma_{\mathrm{in}}} = \boldsymbol{0},\, \boldsymbol{f}\cdot\boldsymbol{n}|_{\Gamma_{\mathrm{lat}}} = 0 \Big\},$$
$$\mathcal{P}^f = \Big\{ f \in \mathcal{L}^2(\mathbb{R}^d) \Big\}, \quad \mathcal{I}^\Gamma = \Big\{ \boldsymbol{f} \in \mathcal{H}^{1/2}(\Gamma) \Big\}, \quad \text{and} \quad \mathcal{I} = \Big\{ \boldsymbol{f} \in \mathcal{H}^1(\mathbb{R}^d) \Big\},$$
$$\mathcal{U}^s_0 = \Big\{ \boldsymbol{f} \in \mathcal{H}^1(\Omega_{\mathrm{s}}),\, \boldsymbol{f}|_{\partial\Omega_{\mathrm{s}}\setminus\Gamma} = \boldsymbol{0} \Big\}, \quad \mathcal{U}^e_0 = \Big\{ \boldsymbol{f} \in \mathcal{H}^1(\Omega_{\mathrm{e}}),\, \boldsymbol{f}|_{\partial\Omega_{\mathrm{e}}\setminus\Gamma} = \boldsymbol{0},\, \text{zero-extension in } \Omega_{\mathrm{f}}\setminus\Omega_{\mathrm{e}} \Big\}.$$

In the above definitions, both $\mathcal{U}^f/\mathcal{U}^f_0$ (space for the fluid velocity), $\mathcal{P}^f$ (space for the fluid pressure), $\mathcal{I}$ space for the Lagrange multipliers are independent from $\boldsymbol{\theta}$. The space for the solid displacement/velocity, $\mathcal{U}^s_0$, depends explicitly on Ω_{s} which does not depend on $\boldsymbol{\theta}$. The same is true for the space $\mathcal{U}^e_0$ for the extension displacement.

The Lagrangian function associated to the steady problem is written on the form of the variational formulation of the steady Navier-Stokes with Lagrange multiplier on the interface [56, 57]. Introducing the direct and adjoint variables $[\boldsymbol{U}, P, \boldsymbol{\Lambda}] \in \mathcal{U}^f \times \mathcal{P}^f \times \mathcal{I}$ and $[\boldsymbol{U}^\dagger, P^\dagger, \boldsymbol{\Lambda}^\dagger] \in \mathcal{U}^f_0 \times \mathcal{P}^f \times \mathcal{I}$, we set

$$\begin{aligned}\mathscr{L}_s(\boldsymbol{\theta}, [\boldsymbol{U}, P, \boldsymbol{\Lambda}], [\boldsymbol{U}^\dagger, P^\dagger, \boldsymbol{\Lambda}^\dagger]) = &\int_{\Omega_{\mathrm{f}}(\boldsymbol{\theta})} \Big\{ \nabla\boldsymbol{U}\,\boldsymbol{U}\cdot\overline{\boldsymbol{U}}^\dagger + \frac{2}{\mathcal{R}_{\mathrm{e}}}\mathbf{D}(\boldsymbol{U}) : \nabla\overline{\boldsymbol{U}}^\dagger - \big(\nabla\cdot\boldsymbol{U}\,\overline{P}^\dagger + \nabla\cdot\overline{\boldsymbol{U}}^\dagger\, P\big) \Big\}\,\mathrm{d}\Omega \\ &- \int_{\Gamma_{\mathrm{rgd}}(\boldsymbol{\theta})\cup\Gamma} \Big\{ \boldsymbol{U}\cdot\overline{\boldsymbol{\Lambda}}^\dagger + \boldsymbol{\Lambda}\cdot\overline{\boldsymbol{U}}^\dagger \Big\}\,\mathrm{d}\Gamma.\end{aligned} \tag{A.1}$$

We have considered here an hermitian scalar product (hence the complex-conjugates $\overline{\bullet}$), because the adjoint fields are complex [37]. Looking for the conditions for which the variations of $\mathscr{L}_s$ with respect to variables $\boldsymbol{U}^\dagger$, $P^\dagger$ and $\boldsymbol{\Lambda}^\dagger$ are zero give the steady Navier-Stokes equations (2) as well as the no-slip condition (3). Furthermore, we then obtain an expression for the Lagrange multiplier $\boldsymbol{\Lambda}$, namely

$$\boldsymbol{\Lambda} = \boldsymbol{\sigma}(\boldsymbol{U}, P)\boldsymbol{n} \quad \text{on} \quad \Gamma_{\mathrm{rgd}}(\boldsymbol{\theta}) \cup \Gamma. \tag{A.2}$$

Of course, the steady flow variables $[\boldsymbol{U}, P, \boldsymbol{\Lambda}]$ are real fields: since the inflow condition is a real-valued function, the imaginary part of the steady flow variables is identically zero.

Turning now on the unsteady part of the problem, we introduce the fluid perturbations variables $[\boldsymbol{u}^\circ, p^\circ, \boldsymbol{\lambda}^\circ] \in \mathcal{U}^f_0 \times \mathcal{P} \times \mathcal{I}$ and adjoint perturbations $[\boldsymbol{u}^\dagger, p^\dagger, \boldsymbol{\lambda}^\dagger] \in \mathcal{U}^f_0 \times \mathcal{P} \times \mathcal{I}$, the solid perturbations variables $[\boldsymbol{\xi}^\circ, \boldsymbol{u}^\circ_s] \in \mathcal{U}^s_0 \times \mathcal{U}^s_0$ and adjoint perturbations $[\boldsymbol{\xi}^\dagger, \boldsymbol{u}^\dagger_s] \in \mathcal{U}^s_0 \times \mathcal{U}^s_0$, split between the solid displacement and solid velocity, and the extension perturbations $[\boldsymbol{\xi}^\circ_e, \boldsymbol{\lambda}^\circ_e] \in \mathcal{I}^\Gamma \times \mathcal{U}^e_0$ and adjoint extension perturbations $[\boldsymbol{\xi}^\dagger_e, \boldsymbol{\lambda}^\dagger_e] \in \mathcal{I}^\Gamma \times \mathcal{U}^e_0$.

$$
\begin{aligned}
&\mathscr{L}_u(\boldsymbol{\theta},\lambda,\boldsymbol{U},P,[\boldsymbol{\xi}^\circ,\boldsymbol{u}_s^\circ],[\boldsymbol{\xi}_e^\circ,\boldsymbol{\lambda}_e^\circ],[\boldsymbol{u}^\circ,p^\circ,\boldsymbol{\lambda}^\circ],[\boldsymbol{\xi}^\dagger,\boldsymbol{u}_s^\dagger],[\boldsymbol{\xi}_e^\dagger,\boldsymbol{\lambda}_e^\dagger][\boldsymbol{u}^\dagger,p^\dagger,\boldsymbol{\lambda}^\dagger]) = \cdots \\
&\quad \lambda \int_{\Omega_\mathrm{f}(\boldsymbol{\theta})} \Big\{ \boldsymbol{u}^\circ - (\nabla \boldsymbol{U})\boldsymbol{\xi}_e^\circ \Big\} \cdot \overline{\boldsymbol{u}}^\dagger \,\mathrm{d}\Omega + \int_{\Omega_\mathrm{f}(\boldsymbol{\theta})} \Big\{ (\nabla \boldsymbol{U})\boldsymbol{u}^\circ + (\nabla \boldsymbol{u}^\circ)\boldsymbol{U} + (\nabla \boldsymbol{U})\,\boldsymbol{\Phi}'(\boldsymbol{\xi}_e^\circ)\,\boldsymbol{U} \Big\} \cdot \overline{\boldsymbol{u}}^\dagger \,\mathrm{d}\Omega \\
&\quad + \frac{2}{\mathcal{R}_\mathrm{e}} \int_{\Omega_\mathrm{f}(\boldsymbol{\theta})} \Big\{ \mathbf{D}(\boldsymbol{U})\boldsymbol{\Phi}'(\boldsymbol{\xi}_e^\circ)^\mathrm{T} - \frac{1}{2}\big(\nabla \boldsymbol{U} \nabla \boldsymbol{\xi}_e^\circ + \nabla \boldsymbol{\xi}_e^{\circ\,\mathrm{T}} \nabla \boldsymbol{U}^\mathrm{T}\big) + \mathbf{D}(\boldsymbol{u}^\circ) \Big\} : \nabla \overline{\boldsymbol{u}}^\dagger \mathrm{d}\Omega \\
&\quad - \int_{\Omega_\mathrm{f}(\boldsymbol{\theta})} \Big\{ \big(\nabla \cdot \boldsymbol{u}^\circ\, \overline{p}^\dagger + \nabla \cdot \overline{\boldsymbol{u}}^\dagger\, p^\circ\big) + \boldsymbol{\Phi}'(\boldsymbol{\xi}_e^\circ)^\mathrm{T} : \Big(\nabla \boldsymbol{U}\, \overline{p}^\dagger + \nabla \overline{\boldsymbol{u}}^\dagger\, P \Big) \Big\} \mathrm{d}\Omega - \int_{\Gamma \cup \Gamma_\mathrm{rgd}(\boldsymbol{\theta})} \boldsymbol{\lambda}^\circ \cdot \overline{\boldsymbol{u}}^\dagger \,\mathrm{d}\Gamma \\
&\quad + \lambda \int_{\Omega_\mathrm{s}} \Big\{ \mathcal{M}_\mathrm{s}\, \boldsymbol{u}_s^\circ \cdot \overline{\boldsymbol{u}}_s^\dagger + \boldsymbol{\xi}^\circ \cdot \overline{\boldsymbol{\xi}}^\dagger \Big\} \mathrm{d}\Omega + \int_{\Omega_\mathrm{s}} \Big\{ \boldsymbol{\sigma}_\mathrm{s}(\boldsymbol{\xi}^\circ) : \nabla \overline{\boldsymbol{u}}_s^\dagger - \boldsymbol{u}_s^\circ \cdot \overline{\boldsymbol{\xi}}^\dagger \Big\} \mathrm{d}\Omega + \int_\Gamma \boldsymbol{\lambda}^\circ \cdot \overline{\boldsymbol{u}}_s^\dagger \,\mathrm{d}\Gamma \\
&\quad + \int_{\Omega_\mathrm{e}} \Big\{ \nabla \boldsymbol{\xi}_e^\circ : \nabla \overline{\boldsymbol{\xi}}_e^\dagger \Big\} \mathrm{d}\Omega - \int_\Gamma \boldsymbol{\lambda}_e^\circ \cdot \overline{\boldsymbol{\xi}}_e^\dagger \,\mathrm{d}\Gamma \\
&\quad + \int_\Gamma \Big\{ \boldsymbol{\xi}^\circ - \boldsymbol{\xi}_e^\circ \Big\} \cdot \overline{\boldsymbol{\lambda}}_e^\dagger \,\mathrm{d}\Gamma + \int_\Gamma \Big\{ \lambda\, \boldsymbol{\xi}^\circ - \boldsymbol{u}^\circ \Big\} \cdot \overline{\boldsymbol{\lambda}}^\dagger \,\mathrm{d}\Gamma + \int_{\Gamma_\mathrm{rgd}(\boldsymbol{\theta})} \Big\{ \mathbf{0} - \boldsymbol{u}^\circ \Big\} \cdot \overline{\boldsymbol{\lambda}}^\dagger \,\mathrm{d}\Gamma
\end{aligned}
\tag{A.3}
$$

Looking for the conditions for which the variations of $\mathscr{L}_s$ with respect to adjoint fluid perturbation variables $\boldsymbol{u}^\dagger$, $p^\dagger$ and $\boldsymbol{\lambda}^\dagger$ allow to recover the fluid momentum and continuity equations (7) and (8) (first three lines in (A.3)), as well as the velocity interface condition (11). Taking the variations with respect to the solid perturbation variables $\boldsymbol{u}_s^\dagger$ and $\boldsymbol{\xi}^\dagger$ give the solid momentum and velocity equations (4) and (5) repectively (fourth line). Finally, takeing the variations with respect to the extension perturbation variables $\boldsymbol{\xi}_e^\dagger$ and $\boldsymbol{\lambda}_e^\dagger$ allow to recover the extension equation (13) and the interface displacement condition (10), and also gives $\boldsymbol{\lambda}_e^\circ = \nabla \boldsymbol{\xi}_e^\circ\, \boldsymbol{n}$ on Γ. Eventually, because $\boldsymbol{u}_s^\circ = \boldsymbol{u}^\circ$ on Γ, we also obtain that

$$
\boldsymbol{\lambda}^\circ = \big(\boldsymbol{\Sigma}'(\boldsymbol{\xi}_e^\circ, \boldsymbol{U}, P) + \boldsymbol{\sigma}(\boldsymbol{u}^\circ, p^\circ)\big)\boldsymbol{n} = \boldsymbol{\sigma}_\mathrm{s}(\boldsymbol{\xi}^\circ)\boldsymbol{n} \quad \text{on} \quad \Gamma \qquad \text{and} \qquad \boldsymbol{\lambda}^\circ = \boldsymbol{\sigma}(\boldsymbol{u}^\circ, p^\circ)\boldsymbol{n} \quad \text{on} \quad \Gamma_\mathrm{rgd}(\boldsymbol{\theta}). \tag{A.4}
$$

The interface stress condition (12) is thus implicitly satisfied, as was already done for instance in [23, 58].

Following for instance Marquet et al. [37], a complex Lagrangian function for the shape optimization problem is introduced as follows:

$$
\begin{aligned}
&\mathscr{L}(\boldsymbol{\theta},\lambda,[\boldsymbol{U},P,\boldsymbol{\Lambda}],[\boldsymbol{\xi}^\circ,\boldsymbol{u}_s^\circ],[\boldsymbol{\xi}_e^\circ,\boldsymbol{\lambda}_e^\circ],[\boldsymbol{u}^\circ,p^\circ,\boldsymbol{\lambda}^\circ],[\boldsymbol{\xi}^\dagger,\boldsymbol{u}_s^\dagger],[\boldsymbol{\xi}_e^\dagger,\boldsymbol{\lambda}_e^\dagger][\boldsymbol{u}^\dagger,p^\dagger,\boldsymbol{\lambda}^\dagger]) = \\
&\qquad \lambda \\
&\qquad - \mathscr{L}_s(\boldsymbol{\theta},[\boldsymbol{U},P,\boldsymbol{\Lambda}],[\boldsymbol{U}^\dagger,P^\dagger,\boldsymbol{\Lambda}^\dagger]) \\
&\qquad - \mathscr{L}_u(\boldsymbol{\theta},\lambda,\boldsymbol{U},P,[\boldsymbol{\xi}^\circ,\boldsymbol{u}_s^\circ],[\boldsymbol{\xi}_e^\circ,\boldsymbol{\lambda}_e^\circ],[\boldsymbol{u}^\circ,p^\circ,\boldsymbol{\lambda}^\circ],[\boldsymbol{\xi}^\dagger,\boldsymbol{u}_s^\dagger],[\boldsymbol{\xi}_e^\dagger,\boldsymbol{\lambda}_e^\dagger][\boldsymbol{u}^\dagger,p^\dagger,\boldsymbol{\lambda}^\dagger]).
\end{aligned}
\tag{A.5}
$$

This formulation allows to use classical optimization results [59, 10]: the gradient is obtain from a differentiation of $\mathscr{L}$ with respect to the Lagrangian mapping $\boldsymbol{\theta}$. It is found to depend on the direct and adjoint fields. Equations for these fields are obtained by setting all partial derivatives of the Lagrangian to zero, namely

- $\big\{\partial\mathscr{L}/\partial[\boldsymbol{U}^\dagger,P^\dagger,\boldsymbol{\Lambda}^\dagger]\big\}\,(\delta\boldsymbol{U}^\dagger,\delta P^\dagger,\delta\boldsymbol{\Lambda}^\dagger) = 0$: direct stationary flow equations,
- $\big\{\partial\mathscr{L}/\partial[\boldsymbol{\xi}^\dagger,\boldsymbol{u}_s^\dagger,\boldsymbol{\xi}_e^\dagger,\boldsymbol{\lambda}_e^\dagger,\boldsymbol{u}^\dagger,p^\dagger,\boldsymbol{\lambda}^\dagger]\big\}(\delta\boldsymbol{\xi}^\dagger,\delta\boldsymbol{u}_s^\dagger,\delta\boldsymbol{\xi}_e^\dagger,\delta\boldsymbol{\lambda}_e^\dagger,\delta\boldsymbol{u}^\dagger,\delta p^\dagger,\delta\boldsymbol{\lambda}^\dagger) = 0$: fluid-solid eigenvalue problem,
- $\big\{\partial\mathscr{L}/\partial[\boldsymbol{\xi}^\circ,\boldsymbol{u}_s^\circ,\boldsymbol{\xi}_e^\circ,\boldsymbol{\lambda}_e^\circ,\boldsymbol{u}^\circ,p^\circ,\boldsymbol{\lambda}^\circ]\big\}(\delta\boldsymbol{\xi}^\circ,\delta\boldsymbol{u}_s^\circ,\delta\boldsymbol{\xi}_e^\circ,\delta\boldsymbol{\lambda}_e^\circ,\delta\boldsymbol{u}^\circ,\delta p^\circ,\delta\boldsymbol{\lambda}^\circ) = 0$: adjoint eigenvalue problem,
- $\partial\mathscr{L}/\partial\lambda = 0$: direct/adjoint modes normalization,
- $\big\{\partial\mathscr{L}/\partial[\boldsymbol{U},P,\boldsymbol{\Lambda}]\big\}\,(\delta\boldsymbol{U},\delta P,\delta\boldsymbol{\Lambda}) = 0$: adjoint stationary flow equations.

Appendix A.2. Adjoint fluid-solid eigenvalue problem

Equations for the adjoint fluid-solid eigenvalue problem are found by looking for the conditions for which the variations of $\mathscr{L}$ with respect to direct steady variables $\boldsymbol{U}$, P and $\boldsymbol{\Lambda}$ vanish, i.e.

$$\mathscr{L}'(\cdots)(\delta\boldsymbol{\xi}^\circ, \delta\boldsymbol{u}_s^\circ, \delta\boldsymbol{\xi}_e^\circ, \delta\boldsymbol{\lambda}_e^\circ, \delta\boldsymbol{u}^\circ, \delta p^\circ, \delta\boldsymbol{\lambda}^\circ) = 0 \quad \forall\, (\delta\boldsymbol{\xi}^\circ, \delta\boldsymbol{u}_s^\circ, \delta\boldsymbol{\xi}_e^\circ, \delta\boldsymbol{\lambda}_e^\circ, \delta\boldsymbol{u}^\circ, \delta p^\circ, \delta\boldsymbol{\lambda}^\circ)$$

Local equations are found using integration by parts. We use the following identities:

$$\boldsymbol{\Sigma}'(\delta\boldsymbol{\xi}_e^\circ, \boldsymbol{U}, P) : \nabla\overline{\boldsymbol{u}}^\dagger - \boldsymbol{\Phi}'(\boldsymbol{\xi}_e^\circ)^{\mathrm{T}} : \nabla\boldsymbol{U}\,\overline{p}^\dagger = \boldsymbol{\Sigma}^\dagger(\boldsymbol{U}, P, \overline{\boldsymbol{u}}^\dagger, \overline{p}^\dagger) : \nabla\delta\boldsymbol{\xi}_e^\circ$$

where $\boldsymbol{\Sigma}^\dagger(\boldsymbol{U}, P, \overline{\boldsymbol{u}}^\dagger, \overline{p}^\dagger)$ is given by (25). Using integration by parts, and using that $\nabla\cdot\boldsymbol{U} = 0$ in Ω_{f},

$$\begin{aligned}\int_{\Omega_{\mathrm{f}}} \nabla\boldsymbol{U}\,\boldsymbol{\Phi}'(\delta\boldsymbol{\xi}_e^\circ)\boldsymbol{U}\cdot\overline{\boldsymbol{u}}^\dagger\,\mathrm{d}\Omega &= \int_{\partial\Omega_{\mathrm{f}}} \nabla\boldsymbol{U}\,[\boldsymbol{U}\,(\delta\boldsymbol{\xi}_e^\circ\cdot\boldsymbol{n}) - \delta\boldsymbol{\xi}_e^\circ(\boldsymbol{U}\cdot\boldsymbol{n})]\cdot\overline{\boldsymbol{u}}^\dagger\,\mathrm{d}\Gamma \;\cdots\\ &- \int_{\Omega_{\mathrm{f}}} \left\{\nabla\boldsymbol{U}^{\mathrm{T}}\left(\nabla\boldsymbol{U}^{\mathrm{T}}\overline{\boldsymbol{u}}^\dagger - \nabla\overline{\boldsymbol{u}}^\dagger\boldsymbol{U}\right) + (\nabla\overline{\boldsymbol{u}}^\dagger)^{\mathrm{T}}\nabla\boldsymbol{U}\,\boldsymbol{U}\right\}\cdot\delta\boldsymbol{\xi}_e^\circ\,\mathrm{d}\Omega.\end{aligned}$$

and

$$\int_{\Omega_{\mathrm{f}}} \left\{\nabla\boldsymbol{U}\,\boldsymbol{u}^\circ + \nabla\boldsymbol{u}^\circ\,\boldsymbol{U}\right\}\cdot\boldsymbol{u}^\dagger\,\mathrm{d}\Omega = \int_{\Omega_{\mathrm{f}}} \left\{\nabla\boldsymbol{U}^{\mathrm{T}}\,\boldsymbol{u}^\dagger - \nabla\boldsymbol{u}^\dagger\,\boldsymbol{U}\right\}\cdot\boldsymbol{u}^\circ\,\mathrm{d}\Omega + \int_{\partial\Omega_{\mathrm{f}}} (\boldsymbol{U}\cdot\boldsymbol{n})(\boldsymbol{u}^\circ\cdot\boldsymbol{u}^\dagger)\,\mathrm{d}\Gamma.$$

we get

$$\begin{aligned}&\int_{\Omega_{\mathrm{f}}} \left\{\left(\lambda\,\overline{\boldsymbol{u}}^\dagger + (\nabla\boldsymbol{U})^{\mathrm{T}}\overline{\boldsymbol{u}}^\dagger - (\nabla\overline{\boldsymbol{u}}^\dagger)\boldsymbol{U}\right)\cdot\delta\boldsymbol{u}^\circ + \boldsymbol{\sigma}(\overline{\boldsymbol{u}}^\dagger, \overline{p}^\dagger) : \nabla\delta\boldsymbol{u}^\circ\right\}\mathrm{d}\Omega + \int_{\Gamma_{\mathrm{out}}} (\boldsymbol{U}\cdot\boldsymbol{n})(\overline{\boldsymbol{u}}^\dagger\cdot\delta\boldsymbol{u}^\circ)\mathrm{d}\Gamma\\
&- \int_{\Omega_{\mathrm{f}}} \nabla\cdot\overline{\boldsymbol{u}}^\dagger\,\delta p^\circ\,\mathrm{d}\Gamma\\
&- \int_{\Omega_{\mathrm{e}}} \left\{\left(\lambda\,(\nabla\boldsymbol{U})^{\mathrm{T}}\overline{\boldsymbol{u}}^\dagger + (\nabla\boldsymbol{U})^{\mathrm{T}}\left((\nabla\boldsymbol{U})^{\mathrm{T}}\overline{\boldsymbol{u}}^\dagger - (\nabla\overline{\boldsymbol{u}}^\dagger)\boldsymbol{U}\right) + (\nabla\overline{\boldsymbol{u}}^\dagger)^{\mathrm{T}}(\nabla\boldsymbol{U})\boldsymbol{U}\right)\cdot\delta\boldsymbol{\xi}_e^\circ - \left(\boldsymbol{\Sigma}^\dagger(\boldsymbol{U}, P, \overline{\boldsymbol{u}}^\dagger, \overline{p}^\dagger) + \nabla\overline{\boldsymbol{\xi}}_e^\dagger\right) : \nabla\boldsymbol{\xi}_e^\circ\right\}\mathrm{d}\Omega\\
&+ \int_{\Omega_{\mathrm{s}}} \left\{\left(\lambda\mathcal{M}_{\mathrm{s}}\,\overline{\boldsymbol{u}}_s^\dagger - \overline{\boldsymbol{\xi}}^\dagger\right)\cdot\delta\boldsymbol{u}_s^\circ + \lambda\,\overline{\boldsymbol{\xi}}^\dagger\cdot\nabla\boldsymbol{\xi}^\circ + \boldsymbol{\sigma}_{\mathrm{s}}(\overline{\boldsymbol{u}}_s^\dagger) : \nabla\delta\boldsymbol{\xi}^\circ\right\}\mathrm{d}\Omega\\
&- \int_\Gamma \overline{\boldsymbol{\xi}}_e^\dagger\cdot\delta\boldsymbol{\lambda}_e^\circ\,\mathrm{d}\Gamma + \int_\Gamma \left(\lambda\,\overline{\boldsymbol{\lambda}}^\dagger + \overline{\boldsymbol{\lambda}}_e^\dagger\right)\cdot\delta\boldsymbol{\xi}^\dagger\,\mathrm{d}\Gamma - \int_\Gamma \overline{\boldsymbol{\lambda}}_e^\dagger\cdot\delta\boldsymbol{\xi}_e^\circ\,\mathrm{d}\Gamma - \int_{\Gamma\cup\Gamma_{\mathrm{rgd}}} \overline{\boldsymbol{\lambda}}^\dagger\cdot\delta\boldsymbol{u}^\circ\,\mathrm{d}\Gamma\\
&+ \int_\Gamma \left(\overline{\boldsymbol{u}}_s^\dagger - \overline{\boldsymbol{u}}^\dagger\right)\cdot\delta\boldsymbol{\lambda}^\dagger\,\mathrm{d}\Gamma + \int_{\Gamma_{\mathrm{rgd}}} \overline{\boldsymbol{u}}^\dagger\cdot\delta\boldsymbol{\lambda}^\dagger\,\mathrm{d}\Gamma = 0 \quad \forall\,(\delta\boldsymbol{\xi}^\circ, \delta\boldsymbol{u}_s^\circ, \delta\boldsymbol{\xi}_e^\circ, \delta\boldsymbol{\lambda}_e^\circ, \delta\boldsymbol{u}^\circ, \delta p^\circ, \delta\boldsymbol{\lambda}^\circ)\end{aligned}$$

Integrating the above relation by parts, and requiring that the surface integrals vanish, we obtain that on Γ,

$$\begin{aligned}\boldsymbol{\lambda}_e^\dagger + \overline{\lambda}\boldsymbol{\lambda}^\dagger - \boldsymbol{\sigma}_{\mathrm{s}}(\boldsymbol{u}_s^\dagger)\boldsymbol{n} &= 0,\\ -\overline{\boldsymbol{\lambda}}_e^\dagger + \left(\boldsymbol{\Sigma}^\dagger(\boldsymbol{U}, P, \overline{\boldsymbol{u}}^\dagger, \overline{p}^\dagger) + \nabla\overline{\boldsymbol{\xi}}_e^\dagger\right)\boldsymbol{n} &= 0,\\ -\overline{\boldsymbol{\lambda}}^\dagger + \boldsymbol{\sigma}(\boldsymbol{u}^\dagger, p^\dagger)\boldsymbol{n} &= 0.\end{aligned}$$

Appendix A.3. Adjoint steady flow

Equations for the adjoint steady flow are found by looking for the conditions for which the variations of $\mathscr{L}$ with respect to direct steady variables $\boldsymbol{U}$, P and $\boldsymbol{\Lambda}$ vanish, i.e.

$$\mathscr{L}'(\cdots)(\delta\boldsymbol{U}, \delta P, \delta\boldsymbol{\Lambda}) = 0 \quad \forall\,(\delta\boldsymbol{U}, \delta P, \delta\boldsymbol{\Lambda}) \in \mathcal{U}_0^f \times \mathcal{P}^f \times \mathcal{I}.$$

Unlike for the perturbation fields, both $\mathscr{L}_s$ and $\mathscr{L}_u$ depend on the steady variables. From (A.1) and (A.3) we obtain

$$
\begin{aligned}
&\int_{\Omega_\mathrm{f}} \Big\{ \big(\nabla\delta\boldsymbol{U}\,\boldsymbol{U} + \nabla\boldsymbol{U}\,\delta\boldsymbol{U}\big)\cdot\overline{\boldsymbol{U}}^\dagger + \frac{2}{\mathcal{R}_\mathrm{e}}\mathbf{D}(\delta\boldsymbol{U}) : \nabla\overline{\boldsymbol{U}}^\dagger - \big(\nabla\cdot\delta\boldsymbol{U}\,\overline{P}^\dagger + \nabla\cdot\overline{\boldsymbol{U}}^\dagger\,\delta P\big)\Big\}\,\mathrm{d}\Omega \\
&- \int_{\Gamma_{\mathrm{rgd}}\cup\Gamma} \Big\{\delta\boldsymbol{U}\cdot\overline{\boldsymbol{\Lambda}}^\dagger + \delta\boldsymbol{\Lambda}\cdot\overline{\boldsymbol{U}}^\dagger\Big\}\,\mathrm{d}\Gamma \\
&= \int_{\Omega_\mathrm{f}} \Big\{(\nabla\delta\boldsymbol{U})\big(\lambda\,\boldsymbol{\xi}_e^\circ - \boldsymbol{u}^\circ - \boldsymbol{\Phi}'(\boldsymbol{\xi}_e^\circ)\,\boldsymbol{U}\big) - \big(\nabla\boldsymbol{u}^\circ - (\nabla\boldsymbol{U})\,\boldsymbol{\Phi}'(\boldsymbol{\xi}_e^\circ)\big)\delta\boldsymbol{U}\Big\}\cdot\overline{\boldsymbol{u}}^\dagger\,\mathrm{d}\Omega \\
&- \frac{2}{\mathcal{R}_\mathrm{e}}\int_{\Omega_\mathrm{f}} \Big\{\mathbf{D}(\delta\boldsymbol{U})\boldsymbol{\Phi}'(\boldsymbol{\xi}_e^\circ)^\mathrm{T} - \frac{1}{2}\big(\nabla\delta\boldsymbol{U}\nabla\boldsymbol{\xi}_e^\circ + \nabla\boldsymbol{\xi}_e^{\circ\,\mathrm{T}}\nabla\delta\boldsymbol{U}^\mathrm{T}\big)\Big\} : \nabla\overline{\boldsymbol{u}}^\dagger\mathrm{d}\Omega \\
&+ \int_{\Omega_\mathrm{f}} \boldsymbol{\Phi}'(\boldsymbol{\xi}_e^\circ)^\mathrm{T} : \Big(\nabla\delta\boldsymbol{U}\,\overline{p}^\dagger + \nabla\overline{\boldsymbol{u}}^\dagger\,\delta P\Big)\mathrm{d}\Omega \qquad \forall\,(\delta\boldsymbol{U},\delta P,\delta\boldsymbol{\Lambda}) \in \mathcal{U}_0^f\times\mathcal{P}^f\times\mathcal{I}.
\end{aligned}
$$

The left-hand side of the above relation corresponds to the linearized Navier-Stokes equations with interface Lagrange multipliers, for which the manipulations leading to the adjoint system are standard [60, 44, 37, 43]. For the left-hand side, we will use the three following identities to "factorize" by the variation variables:

$$
\begin{aligned}
&\boldsymbol{\Sigma}'(\boldsymbol{\xi}_e^\circ,\delta\boldsymbol{U},\delta P) : \nabla\overline{\boldsymbol{u}}^\dagger - \boldsymbol{\Phi}'(\boldsymbol{\xi}_e^\circ)^\mathrm{T} : \nabla\delta\boldsymbol{U}\,\overline{p}^\dagger = \boldsymbol{\Sigma}'(\boldsymbol{\xi}_e^\circ,\overline{\boldsymbol{u}}^\dagger,\overline{p}^\dagger) : \nabla\delta\boldsymbol{U} - \boldsymbol{\Phi}'(\boldsymbol{\xi}_e^\circ)^\mathrm{T} : \nabla\overline{\boldsymbol{u}}^\dagger\,\delta P, \\
&\big(\nabla\boldsymbol{u}^\circ - (\nabla\boldsymbol{U})\,\boldsymbol{\Phi}'(\boldsymbol{\xi}_e^\circ)\big)\delta\boldsymbol{U}\cdot\overline{\boldsymbol{u}}^\dagger = \big((\nabla\boldsymbol{u}^\circ)^\mathrm{T} - \boldsymbol{\Phi}'(\boldsymbol{\xi}_e^\circ)^\mathrm{T}(\nabla\boldsymbol{U})^\mathrm{T}\big)\overline{\boldsymbol{u}}^\dagger\cdot\delta\boldsymbol{U}, \\
&\int_{\Omega_\mathrm{f}} (\nabla\delta\boldsymbol{U})\big(\lambda\,\boldsymbol{\xi}_e^\circ - \boldsymbol{u}^\circ - \boldsymbol{\Phi}'(\boldsymbol{\xi}_e^\circ)\,\boldsymbol{U}\big)\cdot\overline{\boldsymbol{u}}^\dagger\,\mathrm{d}\Omega = \int_{\partial\Omega_\mathrm{f}} (\delta\boldsymbol{U}\cdot\overline{\boldsymbol{u}}^\dagger)\big(\lambda\,\boldsymbol{\xi}_e^\circ - \boldsymbol{u}^\circ - \boldsymbol{\Phi}'(\boldsymbol{\xi}_e^\circ)\boldsymbol{U}\big)\cdot\boldsymbol{n}\,\mathrm{d}\Gamma\ \cdots \\
&\qquad - \int_{\Omega_\mathrm{f}} \Big\{\lambda\,\big(\nabla\cdot\boldsymbol{\xi}_e^\circ\,\overline{\boldsymbol{u}}^\dagger + (\nabla\overline{\boldsymbol{u}}^\dagger)\boldsymbol{\xi}_e^\circ\big) - \nabla\overline{\boldsymbol{u}}^\dagger\big(\boldsymbol{u}^\circ + \boldsymbol{\Phi}'(\boldsymbol{\xi}_e^\circ)\boldsymbol{U}\big)\Big\}\cdot\delta\boldsymbol{U}\,\mathrm{d}\Omega.
\end{aligned}
$$

The two first identities are obtained using tensor indices manipulation. The last one is obtained using integration by parts, the Piola identity $\nabla\cdot\boldsymbol{\Phi}'(\boldsymbol{\xi})^\mathrm{T} = \mathbf{0}$ [61] and the perturbation continuity equation (8). Eventually, the above variational formulation rewrites as

$$
\begin{aligned}
&\int_{\Omega_\mathrm{f}} \Big\{\overline{\big(-\nabla\boldsymbol{U}^\dagger\,\boldsymbol{U} + \nabla\boldsymbol{U}^\mathrm{T}\,\boldsymbol{U}^\dagger\big)}\cdot\delta\boldsymbol{U} + \overline{\Big(-P^\dagger\,\mathbf{I} + \frac{2}{\mathcal{R}_\mathrm{e}}\mathbf{D}(\boldsymbol{U}^\dagger)\Big)} : \nabla\delta\boldsymbol{U} - \overline{\nabla\cdot\boldsymbol{U}^\dagger}\,\delta P\Big)\Big\}\mathrm{d}\Omega \\
&- \int_{\Gamma_{\mathrm{rgd}}\cup\Gamma} \Big\{\delta\boldsymbol{U}\cdot\overline{\boldsymbol{\Lambda}}^\dagger + \delta\boldsymbol{\Lambda}\cdot\overline{\boldsymbol{U}}^\dagger\Big\}\,\mathrm{d}\Gamma + \int_{\Gamma_\mathrm{out}} (\boldsymbol{U}\cdot\boldsymbol{n})(\overline{\boldsymbol{U}}^\dagger\cdot\delta\boldsymbol{U})\mathrm{d}\Gamma \\
&= \int_{\Omega_\mathrm{f}} \overline{\Big\{-(\nabla\overline{\boldsymbol{u}}^\circ)^\mathrm{T}\boldsymbol{u}^\dagger + (\nabla\boldsymbol{u}^\dagger)\overline{\boldsymbol{u}}^\circ - \overline{\lambda}\big(\nabla\cdot\overline{\boldsymbol{\xi}}_e^\circ\,\boldsymbol{u}^\dagger + (\nabla\boldsymbol{u}^\dagger)\overline{\boldsymbol{\xi}}_e^\circ\big) + (\nabla\boldsymbol{u}^\dagger)\boldsymbol{\Phi}'(\overline{\boldsymbol{\xi}}_e^\circ)\,\boldsymbol{U} - \boldsymbol{\Phi}'(\overline{\boldsymbol{\xi}}_e^\circ)^\mathrm{T}(\nabla\boldsymbol{U})^\mathrm{T}\boldsymbol{u}^\dagger\Big\}} \cdot\delta\boldsymbol{U}\,\mathrm{d}\Omega \\
&- \int_{\Gamma_\mathrm{out}} (\boldsymbol{u}^\circ\cdot\boldsymbol{n})(\overline{\boldsymbol{u}}^\dagger\cdot\delta\boldsymbol{U})\mathrm{d}\Gamma \\
&- \int_{\Omega_\mathrm{f}} \overline{\boldsymbol{\Sigma}'(\overline{\boldsymbol{\xi}}_e^\circ,\boldsymbol{u}^\dagger,p^\dagger)} : \nabla\delta\boldsymbol{U}\,\mathrm{d}\Omega + \int_{\Omega_\mathrm{f}} \overline{\boldsymbol{\Phi}'(\overline{\boldsymbol{\xi}}_e^\circ)^\mathrm{T} : \nabla\boldsymbol{u}^\dagger}\,\delta P\,\mathrm{d}\Omega \qquad \forall\,(\delta\boldsymbol{U},\delta P,\delta\boldsymbol{\Lambda}) \in \mathcal{U}_0^f\times\mathcal{P}^f\times\mathcal{I}.
\end{aligned}
$$

Using an integration by parts for the stress terms appearing in the above integrals, we finally arrive to an explicit variational formulation for the adjoint stationary problem, from which we deduce

Appendix A.4. Computation of the shape gradient

The variation with respect to the [domain/interface]

$$\begin{aligned}
\mathscr{L}'(\Gamma_{\mathrm{rgd}})(\delta\boldsymbol{\theta}) = &\int_{\Gamma_{\mathrm{rgd}}} \left\{ \frac{2}{\mathcal{R}_{\mathrm{e}}} \mathbf{D}(\boldsymbol{U}) : \nabla \overline{\boldsymbol{U}}^{\dagger} - \left(\nabla \cdot \boldsymbol{U}\, \overline{P}^{\dagger} + \nabla \cdot \overline{\boldsymbol{U}}^{\dagger}\, P \right) \right\} (\delta\boldsymbol{\theta} \cdot \boldsymbol{n}) \mathrm{d}\Gamma \\
&- \int_{\Gamma_{\mathrm{rgd}}} \left(H + \frac{\partial}{\partial \boldsymbol{n}} \right) \left\{ \boldsymbol{U} \cdot \boldsymbol{\sigma}(\overline{\boldsymbol{U}}^{\dagger}, \overline{P}^{\dagger}) \boldsymbol{n} + \boldsymbol{\sigma}(\boldsymbol{U}, P) \boldsymbol{n} \cdot \overline{\boldsymbol{U}}^{\dagger} \right\} (\delta\boldsymbol{\theta} \cdot \boldsymbol{n}) \mathrm{d}\Gamma \\
&+ \int_{\Gamma_{\mathrm{rgd}}} \left\{ \frac{2}{\mathcal{R}_{\mathrm{e}}} \mathbf{D}(\boldsymbol{u}^{\circ}) : \nabla \overline{\boldsymbol{u}}^{\dagger} - \left(\nabla \cdot \boldsymbol{u}^{\circ}\, \overline{p}^{\dagger} + \nabla \cdot \overline{\boldsymbol{u}}^{\dagger}\, p^{\circ} \right) \right\} (\delta\boldsymbol{\theta} \cdot \boldsymbol{n}) \mathrm{d}\Gamma \\
&- \int_{\Gamma_{\mathrm{rgd}}} \left(H + \frac{\partial}{\partial \boldsymbol{n}} \right) \left\{ \boldsymbol{\sigma}(\boldsymbol{u}^{\circ}, p^{\circ}) \boldsymbol{n} \cdot \overline{\boldsymbol{u}}^{\dagger} + \boldsymbol{u}^{\circ} \cdot \boldsymbol{\sigma}(\overline{\boldsymbol{u}}^{\dagger}, \overline{p}^{\dagger}) \boldsymbol{n} \right\} (\delta\boldsymbol{\theta} \cdot \boldsymbol{n}) \mathrm{d}\Gamma
\end{aligned}$$

Eventually

$$\nabla_{\Omega_{\mathrm{f}}} \lambda = -\frac{2}{\mathcal{R}_{\mathrm{e}}} \mathbf{D}(\boldsymbol{U}) : \mathbf{D}(\overline{\boldsymbol{U}}^{\dagger}) - \frac{2}{\mathcal{R}_{\mathrm{e}}} \mathbf{D}(\boldsymbol{u}^{\circ}) : \mathbf{D}(\overline{\boldsymbol{u}}^{\dagger})$$

References

[1] J.-L. Pfister, O. Marquet, Fluid–structure stability analyses and nonlinear dynamics of flexible splitter plates interacting with a circular cylinder flow, Journal of Fluid Mechanics 896 (2020).

[2] E. de Langre, Fluides et Solides, Éditions de l'École polytechnique, Palaiseau, 2002.

[3] E. H. Dowell, R. Clark, D. Cox, et al., A modern course in aeroelasticity, number 217 in Solid Mechanics and Its Applications, Springer, 2004.

[4] R. T. Haftka, Optimization of flexible wing structures subject to strength and induced drag constraints, AIAA Journal 15 (1977) 1101–1106.

[5] J. Hur, P. Beran, L. Huttsell, R. Snyder, B. Soni, H. Thornburg, Parametric mesh deformation for sensitivity analysis and design of a joined-wing aircraft, 42nd AIAA Aerospace Sciences Meething and Exhibit. Reston: AIAA (2004).

[6] E. Lund, H. Møller, L. A. Jakobsen, Shape design optimization of stationary fluid-structure interaction problems with large displacements, Structural and Multidisciplinary Optimization 25 (2003) 383–392.

[7] N. Aghajari, M. Schäfer, Efficient shape optimization for fluid–structure interaction problems, Journal of Fluids and Structures 57 (2015) 298–313.

[8] J. L. Lions, Optimal control of systems governed by partial differential equations, number 170 in Grundlehren der mathematischen Wissenschaften, Springer Verlag, 1971.

[9] O. Pironneau, On optimum profiles in Stokes flow, Journal of Fluid Mechanics 59 (1973) 117–128.

[10] G. Allaire, M. Schoenauer, Conception optimale de structures, number 58 in Mathématiques et applications, Springer, 2007.

[11] R. Glowinski, O. Pironneau, Towards the computation of minimum drag profiles in viscous laminar flow, Applied Mathematical Modelling 1 (1976) 58–66.

[12] L. Failer, D. Meidner, B. Vexler, Optimal control of a linear unsteady fluid-structure interaction problem, Journal of Optimization Theory and Applications (2016) 1–27.

[13] F. Feppon, G. Allaire, F. Bordeu, J. Cortial, C. Dapogny, Shape optimization of a coupled thermal fluid-structure problem in a level set mesh evolution framework, 2018.

[14] Y. Bazilevs, M.-C. Hsu, M. Bement, Adjoint-based control of fluid-structure interaction for computational steering applications, Procedia Computer Science 18 (2013) 1989–1998.

[15] E. Helgason, S. Krajnović, Optimization using Arbitrary Lagrangian–Eulerian Formulation of the Navier–Stokes equations, Journal of Fluids Engineering 137 (2015) 061202.

[16] J. Heners, L. Radtke, M. Hinze, A. Düster, Adjoint shape optimization for fluid–structure interaction of ducted flows, Computational Mechanics 61 (2018) 259–276.

[17] K. Van der Zee, E. Van Brummelen, I. Akkerman, R. De Borst, Goal-oriented error estimation and adaptivity for fluid–structure interaction using exact linearized adjoints, Computer Methods in Applied Mechanics and Engineering 200 (2011) 2738–2757.

[18] A. Manzoni, L. Ponti, An adjoint-based method for the numerical approximation of shape optimization problems in presence of fluid-structure interaction, 2016.

[19] M. Á. Fernández, P. Le Tallec, Linear stability analysis in fluid-structure interaction with transpiration. Part I: formulation and mathematical analysis, Computer Methods in Applied Mechanics and Engineering 192 (2003) 4805–4835.

[20] M. Á. Fernández, P. Le Tallec, Linear stability analysis in fluid-structure interaction with transpiration. Part II: numerical analysis and applications, Computer Methods in Applied Mechanics and Engineering 192 (2003) 4837–4873.

[21] T. Wick, Fluid-structure interactions using different mesh motion techniques, Computers & Structures 89 (2011) 1456–1467.

[22] T. Wick, W. Wollner, On the differentiability of fluid-structure interaction problems with respect to the problem data (????).

[23] J.-L. Pfister, O. Marquet, M. Carini, Linear stability analysis of strongly coupled fluid–structure problems with the Arbitrary-Lagrangian–Eulerian method, Computer Methods in Applied Mechanics and Engineering (2019).

[24] B. Protas, W. Liao, Adjoint-based optimization of pdes in moving domains, Journal of Computational Physics 227 (2008) 2707–2723.

[25] S. K. Nadarajah, A. Jameson, Optimum shape design for unsteady flows with time-accurate continuous and discrete adjoint method, AIAA Journal 45 (2007) 1478–1491.

[26] E. C. Stewart, M. J. Patil, R. A. Canfield, R. D. Snyder, Aeroelastic shape optimization of a flapping wing, Journal of Aircraft (2016) 636–650.

[27] V. Heuveline, F. Strauß, Shape optimization towards stability in constrained hydrodynamic systems, Journal of Computational Physics 228 (2009) 938–951.

[28] T. Nakazawa, H. Azegami, Shape optimization of flow field improving hydrodynamic stability, Japan Journal of Industrial and Applied Mathematics 33 (2016) 167–181.

[29] Y. Wang, E. Ferrer, A. Martínez-Cava, Y. Zheng, E. Valero, Enhanced stability of flows through contraction channels: Combining shape optimization and linear stability analysis, Physics of Fluids 31 (2019) 074109.

[30] J. Brewster, M. P. Juniper, Shape sensitivity of eigenvalues in hydrodynamic stability, with physical interpretation for the flow around a cylinder, European Journal of Mechanics-B/Fluids 80 (2020) 80–91.

[31] A. Martinez-Cava, M. Chávez-Modena, E. Valero, J. de Vicente, E. Ferrer, Sensitivity gradients of surface geometry modifications based on stability analysis of compressible flows, Physical Review Fluids 5 (2020) 063902.

[32] S. Turek, J. Hron, Proposal for numerical benchmarking of fluid-structure interaction between an elastic object and laminar incompressible flow, in: Fluid-structure interaction, Springer, 2006.

[33] R. Verfürth, Finite element approximation on incompressible navier-stokes equations with slip boundary condition, Numerische Mathematik 50 (1986) 697–721.

[34] D. Sipp, O. Marquet, P. Meliga, A. Barbagallo, Dynamics and control of global instabilities in open-flows: a linearized approach, Applied Mechanics Reviews 63 (2010) 030801.

[35] T. Hughes, W. Liu, T. Zimmermann, Lagrangian-Eulerian finite element formulation for incompressible viscous flows, Computer Methods in Applied Mechanics and Engineering 29 (1981) 329–349.

[36] J. Donea, A. Huerta, J.-P. Ponthot, A. Rodrigez-Ferran, Arbitrary Lagrangian-Eulerian methods, Encyclopedia of Computational Mechanics (2004). URL: http:/dx.doi.org/10.1002/0470091355.ecm009.

[37] O. Marquet, D. Sipp, L. Jacquin, Sensitivity analysis and passive control of cylinder flow, Journal of Fluid Mechanics 615 (2008) 221–252.

[38] A. Henrot, M. Pierre, Variation et optimisation de formes: une analyse géométrique, number 48 in Mathématiques et applications, Springer Science & Business Media, 2006.

[39] M. C. Delfour, J.-P. Zolésio, Shapes and geometries : metrics, analysis, differential calculus, and optimization, Society for Industrial and Applied Mathematics, 2011.

[40] J. Céa, Conception optimale ou identification de formes, calcul rapide de la dérivée directionnelle de la fonction coût, RAIRO-Modélisation mathématique et analyse numérique 20 (1986) 371–402.

[41] J. E. Marsden, T. J. Hughes, Mathematical foundations of elasticity, Dover Books on Mathematics, 1994.

[42] P. Luchini, A. Bottaro, Adjoint equations in stability analysis, Annual Review of Fluid Mechanics 46 (2014) 493.

[43] P. Luchini, A. Bottaro, An introduction to adjoint problems – supplemental appendix to Adjoints equations in stability analysis, Annual Review of Fluid Mechanics 46 (2014) 493.

[44] F. Giannetti, P. Luchini, Structural sensitivity of the first instability of the cylinder wake, Journal of Fluid Mechanics 581 (2006) 167–197.

[45] G. Allaire, O. Pantz, Structural optimization with FreeFem++, Structural and Multidisciplinary Optimization 32 (2006) 173–181.

[46] C. Dapogny, P. Frey, F. Omnès, Y. Privat, Geometrical shape optimization in fluid mechanics using FreeFem++, 2017.

[47] F. Hecht, New development in FreeFem++, Journal of Numerical Mathematics 20 (2012) 251–265.

[48] P. Amestoy, A. Buttari, A. Guermouche, J.-Y. l'Excellent, B. Ucar, MUMPS: a multifrontal massively parallel sparse direct solver, 2013. URL: URl:http:/mumps.enseeiht.fr.

[49] R. Lehoucq, D. Sorensen, C. Yang, ARPACK Users' guide: solution of large scale eigenvalue problems with implicitly restarted Arnoldi methods, 1997. URL: http:/www.caam.rice.edu/software/ARPACK/.

[50] O. Pironneau, Optimal shape design for elliptic systems, Springer Science & Business Media, 2012.

[51] P. Schmid, E. de Langre, Transient growth before coupled-mode flutter, in: ASME 2002 International Mechanical Engineering Congress and Exposition, American Society of Mechanical Engineers, 2002, pp. 1055–1064.

[52] M. Carini, J.-L. Pfister, O. Marquet, Passive control of fluid-structure instabilities by means of piezo-electric shunts, in: 16th European Turbulence Conference, Stockholm, Sweden, 2017. URL: http://w3.onera.fr/erc-aeroflex/sites/w3.onera.fr.erc-aeroflex/files/docs/presentation/carini-pfister-marquet-etc16-2017.pdf.

[53] J. Lee, D. You, Study of vortex-shedding-induced vibration of a flexible splitter plate behind a cylinder, Physics of Fluids 25 (2013) 110811.

[54] J. Wu, Y. Qiu, N. Zhao, Flow control of a circular cylinder by using an attached flexible filament, Physics of Fluids 26 (2014) 103601.

[55] M. S. Mat Ali, C. J. Doolan, V. Wheatley, Low Reynolds number flow over a square cylinder with a splitter plate, Physics of Fluids 23 (2011) 033602.

[56] H. Barbosa, T. Hughes, The finite element method with Lagrange multipliers on the boundary: circumventing the Babŭska-Brezzi condition, Computer Methods in Applied Mechanics and Engineering 85 (1991) 109–128.

[57] I. Babuška, The finite element method with lagrangian multipliers, Numerische Mathematik 20 (1973) 179–192.

[58] S. Deparis, D. Forti, G. Grandperrin, A. Quarteroni, FaCSI: a block parallel preconditioner for fluid–structure interaction in hemodynamics, Journal of Computational Physics 327 (2016) 700–718.

[59] G. Allaire, Analyse numérique et optimisation: une introduction à la modélisation mathématique et à la simulation numérique, 2nd ed., Éditions de l'École polytechnique, Palaiseau, 2012.

[60] O. Pironneau, On optimum design in fluid mechanics, Journal of Fluid Mechanics 64 (1974) 97–110.

[61] P. Chadwick, Continuum mechanics: concise theory and problems, Dover, 1999.